

Randomness-aware multiscale models of glioma invasion and treatment

Martina Conte^{*1}, Sandesh Hiremath², and Christina Surulescu²

¹ *Department of Mathematical Sciences "G.L. Lagrange", Politecnico di Torino
Corso Duca degli Abruzzi, 24 - 10129 Torino, Italy*

² *Department of Mathematics, RPTU Kaiserslautern-Landau
Gottlieb-Daimler-Str. 48 - 67663 Kaiserslautern, Germany*

February 10, 2026

Abstract

In this work, we develop a stochastic multiscale model for glioma growth and invasion in the brain, incorporating the effects of therapeutic interventions. The model accounts for tumor cell migration influenced by brain tissue heterogeneity and anti-crowding mechanisms, while explicitly addressing treatment-related uncertainties through stochastic processes. Starting from a microscopic description of individual cell dynamics, we derive the corresponding system of macroscopic random reaction-diffusion-taxis equations governing cell density and tissue evolution. Finally, we conduct several numerical experiments to assess the efficacy of different treatment protocols, evaluated with respect to both established and newly proposed clinical criteria and measurable outcomes.

Keywords— Glioma multiscale modeling, Kinetic transport equations, Random reaction-diffusion-taxis equations, Radiotherapy, Tumor control probability

1 Introduction

Gliomas are among the most aggressive and infiltrative brain tumors, characterized by complex growth patterns arising from dynamic interactions between tumor cells and their surrounding microenvironment [1], [2]. In particular, gliomas exhibit rapid proliferation and extensive infiltration into healthy brain tissue, which significantly complicates both diagnosis and treatment. Their highly diffusive invasion leads to poorly defined tumor margins, hindering accurate delineation and limiting the extent of safe surgical resection. As a consequence, complete removal of the tumor is rarely possible, and the prognosis for patients remains poor [3], [4].

The first-line treatment for newly diagnosed gliomas typically involves surgical resection of the tumor. However, a complete resection is often impossible because the deeply infiltrative rims cannot be fully characterized with standard medical imaging. For this reason, additional therapies are usually combined with surgery. In particular, radiotherapy is routinely employed to reduce tumor burden (sometimes even prior to surgery) and a variety of radiotherapy protocols have been investigated. Among the most widely studied are hyperfractionated [5], [6] and hypofractionated [7], [8] regimes, which differ in the daily radiation dose delivered to the patient and the resulting overall duration of treatment.

A crucial aspect of all radiotherapy protocols is the presence of substantial uncertainty, which originates from multiple sources. Some of it is due to tumor biology and its microenvironment, including intrinsic variability in radiosensitivity across patients and even within a single tumor, spatial heterogeneity of tissue structure, or fluctuations in nutrient and oxygen availability [9], [10]. Other uncertainties originate from treatment delivery and clinical practice, such as patient-positioning variability, brain shift or fluid accumulation during therapy, missed or delayed treatment sessions, and limitations in imaging resolution or tumor segmentation, among many others [11], [12].

^{*}Corresponding author: martina.conte@polito.it

Understanding glioma progression and elucidating the impact of stochasticity on therapeutic outcomes is therefore essential for designing more reliable and effective treatment strategies.

State of the art Mathematical models of tumor growth and invasion have traditionally been formulated through deterministic partial differential equations (PDEs), which describe cell proliferation, diffusion- and taxis-driven migration, along with further interactions with the surrounding tissue. These models have provided insights into glioma invasion, tissue degradation, and the influence of the microenvironment (e.g., see [13], [14], [15], [16], [17]). However, deterministic frameworks assume that all processes evolve in a predictable manner, which is incompatible with the biological variability observed in clinical settings. Fluctuations in cell motility, tissue properties, and treatment delivery naturally motivate the development of models capable of explicitly incorporating randomness and stochasticity. In recent years, partial differential equations with randomness have been introduced to incorporate stochasticity into continuum tumor models. These approaches have been used to describe random perturbations in cell motility, tumor–tissue interactions, and microenvironmental fields (e.g., see [18], [19], [20], [21], [22], [23], [24], [25], [26]). Such models capture spatial variability in tumor fronts and give rise to more realistic invasive patterns, better reflecting the irregular morphology commonly observed in infiltrative cancers such as gliomas. Notwithstanding these advances, the explicit integration of stochasticity into radiotherapy models has been relatively rarely addressed, in spite of its clinical relevance. Classical mathematical models, including those based on the Linear–Quadratic (LQ) formalism [27], typically treat radiobiological processes deterministically. Yet both experimental and clinical evidence demonstrate substantial variability in radiation response. Only a limited number of recent works have begun to introduce stochastic elements into radiotherapy modeling [28], [29], [30]. These contributions demonstrate that randomness can significantly alter therapeutic predictions, affecting tumor control probability, relapse timing, or trigger the emergence of resistant subpopulations. Nonetheless, most existing models introduce randomness in a phenomenological manner, lacking a systematic multiscale derivation that links microscopic cellular processes to macroscopic tumor evolution.

To capture the multiscale nature of tumor progression, several modeling frameworks have been proposed based on the description of microscopic and/or mesoscale descriptions of cell behavior. Many of these are formulated within the framework of the kinetic theory of active particles (KTAPs) [31], [32], which enables a multiscale representation of multicellular systems. Models within this context characterize cell dynamics at the mesoscopic level, beginning from processes occurring at the scale of individual cells. Through well-established asymptotic techniques, based on diffusive or hydrodynamic scalings, macroscopic equations are derived from these lower-scale descriptions. In the context of glioma modeling, a variety of systems have been proposed on the basis of this approach [33], [34], [35], [36], [37], [38], [39], [40], [41], [42], [43], [44], [45], [46]. Among these, [33], [42] investigate tumor evolution in response to different therapeutic interventions, accounting for their distinct effects on both tumor cells and healthy tissue. However, models that explicitly incorporate multiple therapy approaches remain scarce, and those that directly account for randomness in treatment are even fewer. This gap highlights the need for multiscale PDE frameworks in which stochasticity explicitly enters the radiotherapy terms and propagates through to clinically relevant population-level dynamics. Such models provide a mathematical foundation for randomness-aware predictions of treatment outcomes, facilitate the evaluation of the robustness of treatment protocol, and support the optimization of radiotherapy under realistic variability. The present work contributes towards this aim.

In this work, we develop a multiscale stochastic model for glioma progression and therapy that integrates microscopic, mesoscopic, and macroscopic levels of description using tools from the kinetic theory of active particles. The primary objective is to connect the dynamics of glioma cells and healthy tissue with their responses to therapeutic interventions under inherent randomness. The work is organized as follows. Section 2 presents the formulation of the model at the subcellular and mesoscopic scales and derives the corresponding macroscopic random PDE system. In Section 3 we define the coefficient functions and the initial experimental setup used in the numerical simulations. Section 4 presents the simulation results, evaluating therapy outcomes under various clinically inspired metrics. We conclude with a discussion of the results in Section 5. Additional figures are provided in the Appendix.

2 Model description

This section is dedicated to the development of the stochastic model announced above, with the main goal of characterizing the space-time interactions of glioma cells with surrounding normal tissue and assessing their response to different treatment scenarios under inherent randomness. In the model, glioma cells migrate preferentially along the anisotropic structure of brain tissue while avoiding highly crowded regions. Cell proliferation depends on the availability of surrounding healthy tissue, which supports tumor growth and provides essential supplies. The effects of therapy account for radiation-induced damage to both tumor and normal tissue, though with different sensitivities, and are modulated through a stochastic process of the Ornstein–Uhlenbeck type. This framework enables the assessment of radiotherapy outcomes using the concepts of Tumor Control Probability (TCP), Normal Tissue Complication Probability (NTCP), and Uncomplicated Tumor Control Probability (UTCP), which respectively quantify the probabilities of effective tumor eradication (TCP), of normal tissue damage (NTCP), and of achieving tumor control without inducing severe normal tissue complications (UTCP).

Starting from the microscopic description of interactions between cells and tissue, we formulate the corresponding kinetic transport equations (KTEs) for glioma cells. By performing a formal parabolic scaling limit, we derive the macroscopic random reaction–advection–diffusion equation governing the dynamics of the tumor cell population. Finally, we couple this equation with the ordinary differential equation characterizing evolution of healthy tissue, modeled directly at the macroscopic level.

2.1 Microscopic scale

On the microscopic scale, we describe the interactions between glioma cells, tissue fibers, and the surrounding cellular environment. We assume that cells exchange information with their microenvironment through various types of cell surface receptors. Specifically, the binding of these transmembrane units is considered to trigger intracellular processes that lead to migration and proliferation. This modeling approach follows the ideas introduced in [47], [48] for constructing a multiscale (micro–meso) model of tumor invasion incorporating different types of tactic responses, and subsequently refined in several later works (see [33], [34], [36], [37], [39], [40], [41], [42], [49] and references therein). In particular, this framework enables the inclusion of both single-cell dynamics, that usually appears in the KTEs, and subcellular processes, which have a significant impact on overall tumor progression.

Given the variables for time $t > 0$, spatial position $x \in D \subseteq \mathbb{R}^d$, and microscopic cell velocity $v \in V = s\mathbb{S}^{d-1}$ (namely $v = s\theta$ and $\theta \in \mathbb{S}^{d-1}$, with \mathbb{S}^{d-1} unit sphere in \mathbb{R}^d), we denote by $y_1(t)$ the amount of receptors bound to tissue fibers and by $y_2(t)$ the amount of transmembrane entities mediating adhesion between tumor cells. The corresponding binding dynamics are governed by simple mass-action kinetics:

$$\begin{aligned} (\bar{R}_0 - y_1) + Q &\xrightleftharpoons[k_1^-]{k_1^+} y_1 \\ (\bar{R}_0 - y_2) + M &\xrightleftharpoons[k_2^-]{k_2^+} y_2, \end{aligned}$$

where \bar{R}_0 denotes the total number of receptors on a cell membrane, assumed constant for simplicity. Here, $Q(t, x)$ represents the macroscopic volume fraction of available tissue, irrespective of the orientation of fibers, and $M(t, x)$ the macroscopic tumor cell density. Accordingly, the microscopic receptor-binding dynamics are described by the following system of ordinary differential equations:

$$\begin{aligned} \dot{y}_1 &= k_1^+ Q S_Q(d_r, \boldsymbol{\varrho}_Q)(\bar{R}_0 - y_1) - k_1^- y_1 \\ \dot{y}_2 &= k_2^+ M S_M(d_r, \boldsymbol{\varrho}_M)(\bar{R}_0 - y_2) - k_2^- y_2, \end{aligned} \tag{1}$$

where k_1^+ and k_1^- denote the attachment and detachment rates between tumor cells and tissue fibers, respectively, while k_2^+ and k_2^- correspond to the analogous rates for cell–cell interactions. The factor

$$S_i(d_r, \boldsymbol{\varrho}_i) := \exp(-{}^1\varrho_i d_r - {}^2\varrho_i d_r^2), \quad \boldsymbol{\varrho}_i = [{}^1\varrho_i, {}^2\varrho_i]^\top \tag{2}$$

for $i \in \{Q, M\}$, models the surviving fraction of cells (tumor or healthy) following a radiation dose d_r . This formulation corresponds to the well-known linear–quadratic (LQ) model. Each population affected by radiotherapy is characterized by specific parameters ${}^1\varrho$ and ${}^2\varrho$, which quantify lethal lesions caused by single radiation tracks and by the interaction of two tracks, respectively. A key parameter in this framework is the ratio ${}^1\varrho/{}^2\varrho$, which reflects the cell’s radiosensitivity and correlates with the cell cycle length: late-responding cells with slower proliferation exhibit smaller ${}^1\varrho/{}^2\varrho$ ratios, whereas early-responding, highly aggressive cells display larger ones. The parameters ϱ_M and ϱ_Q denote the effects of radiotherapy on tumor and healthy cells, respectively. In what follows, we refer to S_M and S_Q as the radiotherapy survival fractions corresponding to M and Q , without explicitly indicating their dependence on ϱ , and d_r .

Considering (1), if we assume that $k_1^- = k_2^- = k^-$, then we define $y(t) = y_1(t) + y_2(t)$ the total concentration of bounded receptors on the cell membrane and we lump together the two equations into

$$\dot{y} = (k_1^+ S_Q Q + k_2^+ S_M M) (\bar{R}_0 - y) - k^- y. \quad (3)$$

By rescaling $y/\bar{R}_0 \rightsquigarrow y$, the unique steady state of equation (3) reads

$$y^* = \frac{B(M, Q) - k^-}{B(M, Q)}$$

with

$$B(M, Q) := k_1^+ S_Q Q + k_2^+ S_M M + k^-.$$

We assume that tumor cells tend to migrate along the gradients of tissue fibers while avoiding over-crowded regions. Consequently, we look at the path of a single cell initially located at position x_0 and moving toward position x with velocity v within (locally) time-invariant density fields Q and M , such that $Q(x) = Q(x_0 + vt)$ and $M(x) = M(x_0 - vt)$. Denoting by $z := y^* - y$ the deviation of y from its steady state y^* , we obtain:

$$\dot{z} = -z B(M, Q) + \frac{k^-}{B(M, Q)^2} [k_1^+ S_Q (v \cdot \nabla_x Q + \partial_t Q) - k_2^+ S_M (v \cdot \nabla_x M + \partial_t M)] =: G(z, Q, M).$$

Remark. We remark that the macroscopic densities Q and M depend also on the stochastic realizations $\omega \in \Omega$, hence they are in fact nonnegative stochastic processes defined on $\mathbb{R}_+ \times \Omega$. The whole problem is actually set within the framework of a probability space $(\Omega, \mathcal{F}, \mathbb{P})$, with \mathcal{F} being a filtration and \mathbb{P} the underlying probability measure. These stochastic realizations originate from the randomness contained in the radiotherapy term and therefore propagate up to the macroscopic level. For the sake of clarity, we omit here the explicit dependence on ω ; a detailed handling will be provided in the forthcoming work [50].

2.2 Mesoscopic scale

We model the mesoscale dynamics of glioma cells using kinetic transport equations (KTEs) that describe velocity-jump processes while incorporating microscopic behavior. Specifically, we consider the mesoscopic cell density function $p = p(t, x, v, y)$ which depends on time $t > 0$, spatial position $x \in D \subseteq \mathbb{R}^d$, microscopic velocity $v \in V = s\mathbb{S}^{d-1}$, state variables $y \in Y = (0, 1)$. The choice $v \in V = s\mathbb{S}^{d-1}$ corresponds to tumor cells moving at a constant speed $s > 0$. These choices mean that we assume for tumor cells constant speeds $s > 0$. Following [35], [36], [39], we work with the variable $z = y^* - y \in Z \subseteq (y^* - 1, y^*)$ rather than y itself. The evolution of the glioma cell density is governed by the kinetic transport equation

$$\partial_t p + \nabla_x \cdot (vp) + \partial_z (G(z, Q, M)p) = \mathcal{L}[\lambda(z)]p + \mathcal{P}p - R_M(d_r, \xi_t)p. \quad (4)$$

Here $\mathcal{L}[\lambda(z)]p$ denotes the turning operator, which models changes in cell velocity due to contact guidance, namely the tendency of glioma cells to align with brain tissue anisotropy, primarily along white matter tracts. This operator has a Boltzmann-type integral form:

$$\mathcal{L}[\lambda(z)]p := -\lambda(z)p + \lambda(z) \int_V K(x, v) p(t, x, v', z) dv'.$$

The turning rate $\lambda(z) := \lambda_0 - \lambda_1 z \geq 0$ depends on the microscopic state z , where $\lambda_0 > 0$ and $\lambda_1 > 0$ represent, respectively, the basal turning frequency and the sensitivity to environmental cues. The integral term describes the reorientation of cells from any previous velocity v' to a new velocity v after interacting with the surrounding tissue. The turning kernel $K(x, v)$ is assumed to be independent on v' and characterizes the dominant directional cue imposed by the orientation of tissue fibers. Following [36], [46], we define

$$K(x, v) := \frac{q(x, \theta)}{\gamma}, \quad \theta = \frac{v}{|v|} \in \mathbb{S}^{d-1}, \quad \gamma = s^{d-1},$$

where $q(x, \theta)$ is the orientational distribution function of tissue fibers, normalized by γ . This function encodes patient-specific structural information that can be obtained, in the clinical practice, via diffusion tensor imaging (DTI). In this study, we assume undirected tissue, i.e., $q(x, \theta) = q(x, -\theta)$ for all $x \in \mathbb{R}^d$. A specific choice of $q(x, \theta)$ will be detailed in Section 3. For convenience, we also define:

$$\begin{aligned} \mathbb{E}_q(x) &:= \int_{\mathbb{S}^{d-1}} \theta q(x, \theta) d\theta \\ \mathbb{V}_q(x) &:= \int_{\mathbb{S}^{d-1}} (\theta - \mathbb{E}_q(x)) \otimes (\theta - \mathbb{E}_q(x)) q(x, \theta) d\theta \end{aligned}$$

representing the mean fiber orientation and the variance-covariance matrix of the orientation distribution, respectively. The assumed symmetry of q implies $\mathbb{E}_q = 0$.

As in [33], [37] the term $\mathcal{P} p$ represents the proliferation process induced by receptor-mediated interactions between glioma cells and brain tissue. We define it as

$$\mathcal{P} p := \mu(M, Q) \int_Z \chi(x, z, z') Q(t, x) p(t, x, v, z') dz'.$$

Here, proliferation arises as a consequence of cell-tissue interactions. The proliferation rate $\mu(M, Q)$, depends on both the macroscopic density of tumor cells and the macroscopic density of the surrounding brain tissue. In the integral operator, the kernel $\chi(x, z, z')$ characterizes the transition from state z' to state z during proliferation-triggering events occurring at position x . No further conditions are required on χ ; we only require that the nonlinear proliferative operator be uniformly bounded in the L^2 -norm, which is biologically reasonable given the spatial constraints that limit cell division.

The last term in (4) models the effects of radiotherapy on the tumor cell population as a function of the delivered radiation dose d_r and the stochastic process ξ_t . Specifically, $\xi_t := \xi(t, \omega)$ models treatment-related uncertainties that affect the efficacy of radiation therapy. In clinical practice, such randomness arises from multiple sources, including variability in dose delivery (e.g., fluctuations in beam intensity, energy, or targeting accuracy), patient-specific factors such as anatomical motion, setup and positioning errors, and biological heterogeneity in cell radiosensitivity. Additional variability can result from environmental and technical noise, including equipment calibration errors or imaging inaccuracies [11], [51], [52], [53]. Consequently, ξ_t acts as a common stochastic driver, affecting the entire tumor cell population and representing the aggregate impact of these random fluctuations on the effective radiation response. Incorporating this stochastic term allows the model to capture variability in treatment outcomes, leading to a more robust and clinically relevant description of tumor evolution under radiotherapy. One natural approach to include such stochastic effects in the model is to define the radiotherapy operator as

$$R_M(d_r, \xi_t) := \xi_t \sum_{j=1}^n (1 - S_M(d_r, \varrho_M)) f_\delta(t - t_j) \quad (5)$$

with $S_M(d_r, \varrho_M)$ given in (2). In this formulation, which is reminiscent of its deterministic counterpart in [33], [42], the total dose d_r of the drug is given in smaller fractions, to reduce cytotoxicity. Thereby, n is the number of fractions, while t_j denotes the time instants at which ionizing radiation is applied to the patient. For the function $f_\delta(t - t_j)$ we use an exponential distribution centered at t_j with rate parameter $\delta = 0.001$. This choice allows us to capture the mild temporal propagation of the

radiotherapy effect beyond the effective treatment times t_j . To model the stochastic process ξ_t , we adopt an Ornstein–Uhlenbeck (OU) process which is widely used in radiation modeling to describe mean-reverting random fluctuations in treatment efficacy [54], [55], [56]. The OU process satisfies the stochastic differential equation

$$d\xi_t = (\xi_t - \mu_R)dt + \sigma_R \xi_t dW_t$$

where W_t is a standard Wiener process, μ_R is the expectation of ξ_t , and σ_R is the diffusivity parameter controlling the intensity of random fluctuations.

2.3 Parabolic scaling of the mesoscopic model

As clinicians are primarily interested in the macroscopic evolution of the tumor mass, it is convenient to derive effective equations for the macroscopic dynamics of glioma cells, represented by M . As noted earlier, the equation for the density of healthy tissue Q is already macroscopic and does not require upscaling. The heuristic derivation presented here follows a classical approach; similar methodologies can be found e.g., in [35], [37], [39], [42], [45], [46], [49], [57]. For a rigorous handling unifying parabolic and hyperbolic upscaling for simplified equations, see [58]. We perform a rescaling of time and space as $t \rightarrow \varepsilon^2 t$ and $x \rightarrow \varepsilon x$. In addition, the proliferation term \mathcal{P} and the radiotherapy-induced death term R_M in (4) are scaled by ε^2 to account for mitotic and apoptotic events, which occur on a much longer time scale than cell migration. The rescaled kinetic transport equation for glioma cells then reads:

$$\varepsilon^2 \partial_t p + \varepsilon \nabla_x \cdot (vp) + \partial_z (G(z, Q, M)p) = \mathcal{L}[\lambda(z)]p + \varepsilon^2 \mathcal{P}p - \varepsilon^2 R_M(d_r, \xi_t)p. \quad (6)$$

We define the following moments of the distribution function p :

$$\begin{aligned} m(t, x, v) &= \int_Z p(t, x, v, z) dz & m^z(t, x, v) &= \int_Z z p(t, x, v, z) dz \\ M(t, x) &= \int_V m(t, x, v) dv & M^z(t, x) &= \int_V m^z(t, x, v) dv. \end{aligned}$$

Higher-order moments are neglected based on the assumption that subcellular dynamics occur much faster than events at larger scales, i.e., $z \ll 1$ and that p is compactly supported in the phase space $\mathbb{R}^d \times V \times Z$. Integrating the rescaled equation (6) with respect to z yields

$$\begin{aligned} \varepsilon^2 \partial_t m + \varepsilon \nabla_x \cdot (vm) &= -\lambda_0 \left(m - \frac{q}{\gamma} M \right) + \lambda_1 \left(m^z - \frac{q}{\gamma} M^z \right) \\ &\quad + \varepsilon^2 \int_Z \mu(M) \int_Z \chi(x, z, z') p(z') Q dz' dz - \varepsilon^2 R_M(d_r, \xi_t) m. \end{aligned}$$

Assuming that $\chi(x, z, z')$ is a probability kernel with respect to z for all (x, z') , the first moment equation becomes:

$$\partial_t m + \nabla_x \cdot (vm) = -\lambda_0 \left(m - \frac{q}{\gamma} M \right) + \lambda_1 \left(m^z - \frac{q}{\gamma} M^z \right) + \mu(M) Q m - R_M(d_r, \xi_t) m. \quad (7)$$

Multiplying (6) by z and integrating w.r.t z yields the first-order moment equation in z

$$\varepsilon^2 \partial_t m^z + \varepsilon \nabla_x \cdot (vm^z) + \int_Z z \partial_z [G(z, Q, M)p(z)] dz = \int_Z z \mathcal{L}[\lambda(z)]p(z) dz + \varepsilon^2 \mu(Q) Q m^z - R_M(d_r, \xi_t) m^z.$$

The calculation of the integral term on the left and right hand side leads to the following equation for

$$\begin{aligned} \varepsilon^2 \partial_t m^z + \varepsilon \nabla_x \cdot (vm^z) &= -\lambda_0 \left(m^z - \frac{q}{\gamma} M^z \right) - B(M, Q) m^z + \varepsilon^2 \mu(Q) Q m^z - \varepsilon^2 R_M(d_r, \xi_t) m^z + \\ &\quad \frac{\varepsilon k^-}{B(M, Q)^2} [(k_1^+ S_Q (v \cdot \nabla_x Q + \varepsilon \partial_t Q) - k_2^+ S_M (v \cdot \nabla_x M + \varepsilon \partial_t M)) m]. \end{aligned} \quad (8)$$

We introduce Hilbert expansions for the previously defined moments:

$$\begin{aligned} m(t, x, v) &= \sum_{k=0}^{\infty} \epsilon^k m_k & m^z(t, x, v) &= \sum_{k=0}^{\infty} \epsilon^k m_k^z \\ M(t, x) &= \sum_{k=0}^{\infty} \epsilon^k M_k & M^z(t, x) &= \sum_{k=0}^{\infty} \epsilon^k M_k^z. \end{aligned}$$

Similarly, the proliferation rate is expanded as $\mu(M) = \mu(M_0) + O(\epsilon)$, where M_0 denotes the leading-order macroscopic tumor density, while

$$B(M, Q) = B(M_0, Q) + k_2^+ S_M (M - M_0) + O(|M - M_0|^2)$$

and

$$\frac{1}{B(M, Q)^2} = \frac{1}{B(M_0, Q)^2} - \frac{2k_2^+ S_M}{B(M_0, Q)^3} (M - M_0) + O(|M - M_0|^2).$$

By substituting these expansions into the moment equations (7) and (8), we can systematically collect terms corresponding to each power of ϵ . The resulting hierarchy allows us to derive a macroscopic equation for $M_0(t, x)$ that captures the leading-order dynamics of the glioma cell population. Specifically:

ϵ^0 terms:

$$0 = -\lambda_0 \left(m_0 - \frac{q}{\gamma} M_0 \right) + \lambda_1 \left(m_0^z - \frac{q}{\gamma} M_0^z \right), \quad (9)$$

$$0 = -B(M_0, Q) m_0^z - \lambda_0 \left(m_0^z - \frac{q}{\gamma} M_0^z \right), \quad (10)$$

ϵ^1 terms:

$$\nabla_x \cdot (v m_0) = -\lambda_0 \left(m_1 - \frac{q}{\gamma} M_1 \right) + \lambda_1 \left(m_1^z - \frac{q}{\gamma} M_1^z \right), \quad (11)$$

$$\nabla_x \cdot (v m_0^z) + B(M_0, Q) m_1^z - \frac{k^-}{B(M_0, Q)^2} (k_1^+ S_Q v \cdot \nabla_x Q - k_2^+ S_M v \cdot \nabla_x M_0) m_0 = -\lambda_0 \left(m_1^z - \frac{q}{\gamma} M_1^z \right), \quad (12)$$

ϵ^2 terms:

$$\partial_t m_0 + \nabla_x \cdot (v m_1) = -\lambda_0 \left(m_2 - \frac{q}{\gamma} M_2 \right) + \lambda_1 \left(m_2^z - \frac{q}{\gamma} M_2^z \right) + \mu(M_0) Q m_0 - R_M(d_r, \xi_t) m_0. \quad (13)$$

Integrating (10) with respect to v we have

$$0 = -M_0^z B(M_0, Q) \implies M_0^z = 0. \quad (14)$$

Considering again equation (10) with (14), we have

$$0 = -(B(M_0, Q) + \lambda_0) m_0^z \implies m_0^z = 0. \quad (15)$$

From equation (9), using (14) and (15), we obtain:

$$0 = -\lambda_0 m_0 + \lambda_0 \frac{q}{\gamma} M_0 \implies m_0 = \frac{q}{\gamma} M_0.$$

Considering (12) and integrating it with respect to v , we have

$$\int_V \nabla \cdot (v m_0^z) dv = -B(M_0, Q) M_1^z + \frac{k^-}{B(M_0, Q)^2} \int_V \frac{q}{\gamma} M_0 (k_1^+ S_Q v \cdot \nabla_x Q - k_2^+ S_M v \cdot \nabla_x M_0) dv. \quad (16)$$

In particular, using (15) and the symmetry assumption on the distribution q , equation (16) becomes:

$$0 = -B(M_0, Q)M_1^z \implies M_1^z = 0. \quad (17)$$

Considering again equation (12) and using (17) and (15), we get

$$m_1^z = \frac{k^-}{(B(M_0, Q) + \lambda_0) B(M_0, Q)^2} (k_1^+ S_Q v \cdot \nabla_x Q - k_2^+ S_M v \cdot \nabla_x M_0) m_0.$$

Considering (11) and using (17), we obtain

$$\nabla_x \cdot (v m_0) = -\lambda_0 \left(m_1 - \frac{q}{\gamma} M_1 \right) + \lambda_1 m_1^z \implies \bar{\mathcal{L}}[\lambda_0] m_1 := -\lambda_0 m_1 + \lambda_0 \frac{q}{\gamma} M_1 = \nabla_x \cdot (v m_0) - \lambda_1 m_1^z. \quad (18)$$

In order to get an expression for m_1 we would like to invert the operator $\bar{\mathcal{L}}[\cdot]$. Similar to [36], [46], we define it on the weighted L^2 -space $L_q^2(V)$, in which the measure dv is weighted by $q(x, \theta)/\gamma$. In particular, $L_q^2(V)$ can be decomposed as $L_q^2(V) = \langle q/\gamma \rangle \oplus \langle q/\gamma \rangle^\perp$. For the properties of the chosen turning kernel, $\bar{\mathcal{L}}[\cdot]$ is a compact Hilbert–Schmidt operator with kernel $\langle q/\gamma \rangle$, so that we can compute its pseudo-inverse on $\langle q/\gamma \rangle^\perp$. Thus, to determine m_1 from (18) we verify the solvability condition:

$$\int_V [\nabla_x \cdot (v m_0) - \lambda_1 m_1^z] dv = 0,$$

which holds due to (17) and the assumption of undirected tissue. Consequently, we obtain:

$$m_1 = -\frac{1}{\lambda_0} \left[\nabla_x \cdot (v m_0) - \frac{\lambda_1 k^-}{(B(M_0, Q) + \lambda_0) B(M_0, Q)^2} (k_1^+ S_Q v \cdot \nabla_x Q - k_2^+ S_M v \cdot \nabla_x M_0) m_0 \right]$$

and

$$M_1 = 0. \quad (19)$$

Finally, integrating (13) with respect to v leads to the macroscopic evolution equation:

$$\partial_t M_0 + \int_V \nabla_x \cdot (v m_1) dv = \mu(M_0) Q M_0 - R_M(d_r, \xi_t) M_0$$

with

$$\begin{aligned} \int_V \nabla_x \cdot (v m_1) dv &= \\ \int_V \nabla_x \cdot \left[v \left(-\frac{1}{\lambda_0} \left(\nabla_x \cdot (v m_0) - \frac{\lambda_1 k^-}{(B(M_0, Q) + \lambda_0) B(M_0, Q)^2} (k_1^+ S_Q v \cdot \nabla_x Q - k_2^+ S_M v \cdot \nabla_x M_0) m_0 \right) \right) \right] dv &= \\ \nabla_x \cdot \left[\int_V -\frac{1}{\lambda_0} v \otimes v \nabla_x \cdot \left(\frac{q}{\gamma} M_0 \right) \right] dv + \nabla_x \cdot \left[\frac{\lambda_1 k^- k_1^+ S_Q}{\lambda_0 (B(M_0, Q) + \lambda_0) B(M_0, Q)^2} \int_V v \otimes v \frac{q}{\gamma} dv M_0 \nabla_x Q \right] &- \\ \nabla_x \cdot \left[\frac{\lambda_1 k^- k_2^+ S_M}{\lambda_0 (B(M_0, Q) + \lambda_0) B(M_0, Q)^2} \int_V v \otimes v \frac{q}{\gamma} dv M_0 \nabla_x M_0 \right] &. \end{aligned}$$

Introducing the effective diffusion tensor

$$\mathbb{D}_M(x) := \frac{1}{\lambda_0 \gamma} \int_V v \otimes v q(x, \theta) dv = \frac{s^2}{\lambda_0} \int_{\mathbb{S}^{d-1}} \theta \otimes \theta q(x, \theta) d\theta = s^2 \mathbb{V}_q(x) \quad (20)$$

and, in view of (19), neglecting the ε -correction term for M and the higher order moments, we can write the macroscopic PDE for tumor density $M(t, x)$ as

$$\begin{aligned} \partial_t M - \nabla_x \nabla_x : (\mathbb{D}_M(x) M) + \nabla_x \cdot \left[\frac{\lambda_1 k^-}{(B(M, Q) + \lambda_0) B(M, Q)^2} \mathbb{D}_M(x) (k_1^+ S_Q \nabla_x Q - k_2^+ S_M \nabla_x M) M \right] \\ = (\mu(M) Q - R_M(d_r, \xi_t)) M \end{aligned}$$

where we recall that

$$B(M, Q) = Q S_Q(d_r, \varrho_Q) k_1^+ + M S_M(d_r, \varrho_M) k_2^+ + k^-.$$

In particular, among the various possible expressions for the growth rate $\mu(M)$, following [35], [37], we adopt a logistic-type formulation to account for the self-limiting nature of the growth process:

$$\mu(M) = \mu_M (1 - M) \quad (21)$$

where $\mu_M > 0$ denotes the constant proliferation rate.

The equation for M is coupled with following evolutionary equation for healthy tissue, which is directly stated at the macroscopic level:

$$\partial_t Q = -d_Q \frac{M_0 Q}{1 + M_0} - R_Q(d_r, \xi_t) Q.$$

Here, d_Q is the tumor-mediated tissue degradation rate, and $R_Q(d_r, \xi_t)$ represents the radiotherapy effect on healthy tissue.

Thus, the coupled macroscopic system of stochastic PDEs describing tumor and healthy tissue evolution is:

$$\left\{ \begin{array}{l} \partial_t M - \nabla_x \nabla_x : (\mathbb{D}_M(x) M) + \nabla_x \cdot \left[\frac{\lambda_1 k^-}{(B(M, Q) + \lambda_0) B(M, Q)^2} \mathbb{D}_M(x) (k_1^+ S_Q \nabla_x Q - k_2^+ S_M \nabla_x M) M \right] \\ \quad [\mu_M (1 - M) Q - R_M(d_r, \xi_t)] M, \\ \partial_t Q = -d_Q \frac{M Q}{1 + M} - R_Q(d_r, \xi_t) Q. \end{array} \right. \quad (22)$$

This system has been deduced considering $x \in \mathbb{R}^d$ and it has to be supplemented with adequate initial conditions. For the numerical experiments performed in Section (4) we will consider the system to be set in a bounded, sufficiently regular domain $D \subseteq \mathbb{R}^2$ and endow it with no-flux boundary conditions, which are obtained, e.g. in a similar way to that presented in [59].

3 Assessment of coefficients and set-up of numerical experiments

In this section, we specify the coefficients and functions defining system (22), and we describe the in silico experimental setting used in Section 4.

The computation of the tumor diffusion tensor $\mathbb{D}_M(x)$, introduced in (20), requires prescribing a form for the (mesoscopic) orientational distribution function of tissue fibers, $q(x, \theta)$. Various formulations of this function have been proposed in the literature (see, e.g. [35], [37], [42], [60]). Following [33], [34], we employ the orientation distribution function (ODF), defined as

$$q(x, \theta) = \frac{1}{4\pi |\mathbb{D}_W(x)|^{1/2} (\theta^\top (\mathbb{D}_W(x))^{-1} \theta)^{3/2}}, \quad (23)$$

where $\mathbb{D}_W(x)$ denotes the water diffusion tensor obtained from the patient-specific DTI data. For the radiotherapy terms $R_i(d_r, \xi_t)$, for $i = M, Q$, we recall the general definition (5) and specify

$$R_M(\xi_t) := \xi_t \sum_{j=1}^n \left(1 - S_M(d_r, \varrho_M)\right) f_\delta(t - t_j),$$

$$R_Q(\xi_t) := \xi_t \sum_{j=1}^n \left(1 - S_Q(d_r, \varrho_Q)\right) f_\delta(t - t_j).$$

As described in Section 2.2, for the function $f_\delta(t - t_j)$, we use an exponential distribution with maximum at t_j and having rate parameter $\delta = 0.001$. Regarding the radiation dose, we consider a total dose of $d_r = 60$ Gy, subdivided into a varying number of fractions n according to the specific therapeutic protocol. The radiotherapy parameters ${}^1\varrho_i$ and ${}^2\varrho_i$, which differ between tumor cells ($i = M$) and the healthy tissue ($i = Q$) are listed in Table 1. The growth rate $\mu(M_0)$ has already been introduced in (21). The remaining constant parameters appearing in system (22), together with their ranges and literature sources, are reported in Table 1.

Parameter	Description	Value (unit)	Source
λ_0	basal turning rate	0.001 (s^{-1})	[34], [61]
λ_1	sensitivity to environmental cues	0.001 (s^{-1})	[34], [61]
s	tumor cells speed	$[0.0042, 0.0084] \cdot 10^{-3}$ ($\text{mm} \cdot \text{s}^{-1}$)	[34], [62]
k_1^+	tumor-ECM attachment rate	0.034 (s^{-1})	[34], [63]
k_2^+	cell-cell attachment rate	0.034 (s^{-1})	[63]
k^-	detachment rate	0.01 (s^{-1})	[63]
μ_M	tumor proliferation rate	$[0.11, 9] \cdot 10^{-6}$ (s^{-1})	[64], [65]
${}^1\varrho_M$	single radiation track lesion on tumor	$[0.04, 0.11]$ (Gy^{-1})	[66], [67]
${}^1\varrho_Q$	single radiation track lesion on tissue	0.00025 (Gy^{-1})	[68]
${}^2\varrho_M$	two radiation tracks lesions on tumor	$[0.006, 0.019]$ (Gy^{-2})	[66], [67]
${}^2\varrho_Q$	two radiation tracks lesions on tissue	0.00005 (Gy^{-2})	[68]
d_Q	tissue degradation rate (by acidity)	$[0.06, 8.3] \cdot 10^{-7}$ (s^{-1})	[34]

Table 1: **Model parameters** (dimensional)

3.1 Initial setting

The numerical simulations of the macroscopic system (22) are conducted in a two-dimensional setting to investigate, *in silico*, different scenarios of tumor response to therapy under varying treatment protocols. Simulations are performed using a self-developed MATLAB code (MathWorks, Inc., Natick, MA) and employ the parameters listed in Table 1 and the above defined functions. A Galerkin finite element method is used for spatial discretization [69], while time integration is performed using an IMEX Euler scheme [70], treating the diffusion term implicitly and the drift and reaction terms explicitly. For each treatment protocol, 200 stochastic realizations are computed to account for variability in the simulations.

The computational domain corresponds to a horizontal brain slice reconstructed from MRI data. The macroscopic tensor $\mathbb{D}_M(x)$ is precomputed using DTI data and the ODF defined in (23). The DTI dataset was acquired at the Hospital Galdakao-Usansolo (Galdakao, Spain) and approved by its Ethics Committee; all procedures adhered to institutional guidelines.

The initial conditions are established in two stages. First, we simulate tumor growth in the absence of therapy to generate baseline conditions. Specifically, we initialize a Gaussian-like aggregate

of tumor cells centered at $(x_{0,M}, y_{0,M}) = (-17, 5)$ within the right hemisphere of the brain slice representing our computational domain $D \subseteq \mathbb{R}^2$:

$$M_0(x, y) = e^{\frac{(x-x_{0,M})^2+(y-y_{0,M})^2}{8}}. \quad (24)$$

For the initial distribution of normal tissue, we adopt the formulation from [37]

$$Q_0(x, y) = 1 - \frac{l_c^3(x, y)}{h^3}, \quad (25)$$

where h denotes the voxel side length of the DTI dataset and l_c is a characteristic length estimated as

$$l_c(x, y) = \sqrt{\frac{\text{tr}(\mathbb{D}_W(x, y))h^2}{4l_1}},$$

with l_1 being the leading eigenvalue of the diffusion tensor $\mathbb{D}_W(x, y)$. Here, we use $h = 0.875$ mm, while l_1 is directly estimated from the DTI data in each voxel. To define the initial conditions for treatment simulations, the simulated tumor is first let to evolve without therapeutic intervention for 12 weeks. The resulting tumor distribution at the end of this period serves as the initial condition for treatment assessment. Specifically, in radiotherapy planning, three main volumes are defined [71]. The *Gross Tumor Volume* (GTV) represents the tumor visible on radiological images, where the cancer cell density is highest. The *Clinical Target Volume* (CTV), which cannot be fully imaged, encompasses the GTV plus a margin (typically 2–3 mm) to include potential microscopic disease spread. For example, for high-grade gliomas it is standard practice to apply a uniform margin around the gross tumor to account for microscopic infiltration, regardless of individual considerations. Finally, the *Planning Target Volume* (PTV) extends the CTV by an additional margin (typically 5–10 mm in total from the GTV) to account for geometric and treatment delivery uncertainties. In particular, this is a geometric concept designed to ensure that the radiotherapy dose is actually delivered to the CTV. To replicate clinical practice as closely as possible, we define the GTV at the end of the 12-week untreated growth phase. The GTV corresponds to the imaged tumor, determined using an imaging detection threshold of 16% of the tumor carrying capacity, consistent with the detection limit of T2-Gd MRI [16]. The PTV is then obtained by expanding the GTV uniformly by 5 mm in all directions. This PTV definition is subsequently used to evaluate treatment efficacy metrics. A schematic illustration of this procedure is provided in Figure 1.

4 Numerical experiments and evaluation metrics

In this section, we present the results of the performed numerical tests, outlying for each of the evaluation metrics, the outcomes of the treatment. Specifically, we simulate glioma cell growth and response to therapy under a range of treatment schedules derived from different fractionation protocols, assessing their outcomes through multiple evaluation metrics. The standard radiation protocol is defined as a 6-week course following a 5-days-on, 2-days-off schedule (to account for weekends), delivering a total dose of 60 Gy to the previously defined PTV region. For simplicity, all simulations begin on a Monday, allowing five consecutive treatment days before the two-day rest period. The number of treatment days, denoted as D_T , represents the days on which radiation is actually administered; for the standard protocol, $D_T = 30$.

In clinical settings, radiation is delivered in a full three-dimensional volume; however, in this study we restrict our analysis to two-dimensional cross-sections. Radiotherapy aims to maximize tumor cell kill while minimizing normal tissue toxicity, typically employing daily doses between 1 and 2.5 Gy. Hyper- and hypo-fractionation modify the standard protocol by adjusting dose per fraction and treatment frequency, respectively [72]. Although clinical thresholds for radiation toxicity and necrosis are well established [73], we initially neglect these limits to isolate the effects of accelerated and decelerated schedules on a virtual tumor. This simplification is justified, as techniques such as Gamma Knife radiosurgery [74] can deliver more than 50 Gy in a single session, deliberately trading increased toxicity risk for enhanced local control.

Several fractionation schemes were simulated, corresponding to total treatment durations of $D_T = 15, 20, 25, 30, 35, 40$, and 45 days [14], [72], [75]. In all cases, the maximum total dose within the treatment region was held constant at 60 Gy.

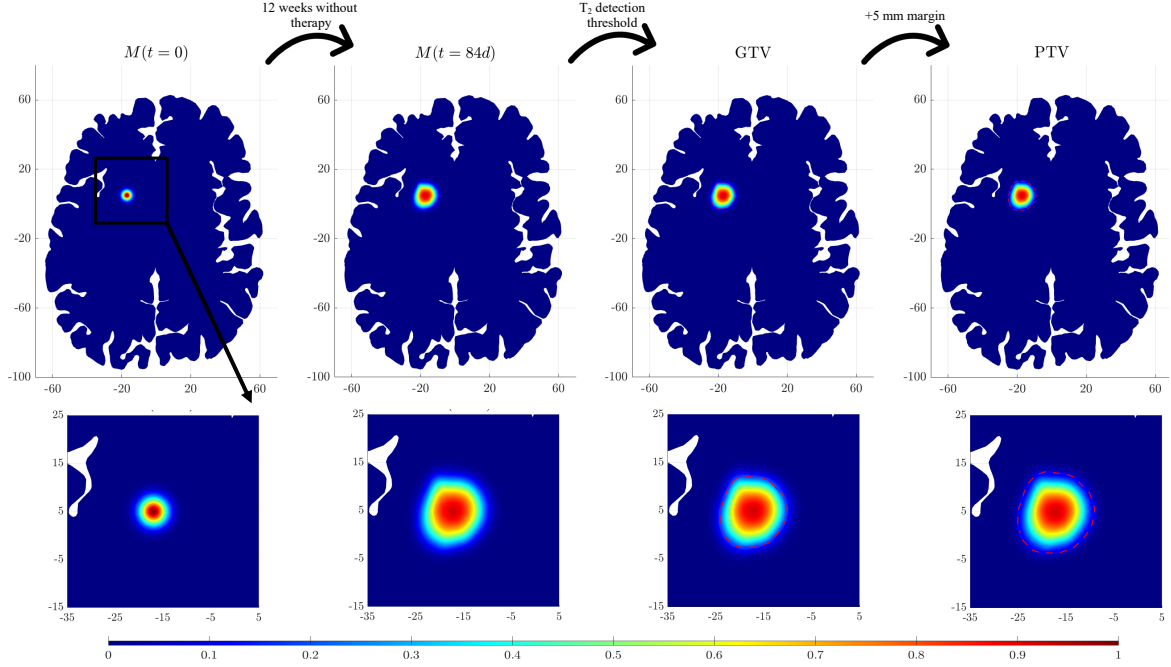


Figure 1: **Definition of the initial setting.** Schematic representation of the model initialization, including the radiotherapy planning volumes. The second row shows magnifications of the main area interested by the tumor mass.

4.1 Impact of detection thresholds on tumor volume estimation

As a first numerical experiment, we analyze and evaluate the effects of the different treatment protocols introduced above, as well as the impact of the detection threshold on their assessment. Clinically, glioma growth and progression are primarily monitored through MRI imaging [76]. Specifically, analyses commonly rely on gadolinium-enhanced T1-weighted (T1Gd) and T2-weighted MRI modalities, which differ in their depiction of tissue contrast. T1Gd images more clearly delineate the bulk of the enhancing lesion, whereas T2-weighted images capture both edema and isolated, sufficiently large tumor cell populations, albeit at a much lower detection threshold. However, all clinical imaging techniques are limited by their sensitivity thresholds, whereas it is well established that glioma cells infiltrate far beyond regions of visible abnormality. We therefore exploit the advantage of *in silico* simulations of radiotherapy, which allow observation of tumor dynamics beyond the clinical detection threshold and enable a clearer comparison between simulated and observable responses.

To this aim, we use the tumor volume (V_T) as the primary response metric, comparing its evolution across the different treatment protocols over a total period of 14 weeks. This time frame includes both the treatment phase (ranging from 3 weeks for $D_T = 15$ to 9 weeks for $D_T = 45$) and the subsequent post-treatment rest period (correspondingly ranging from 11 to 5 weeks). We evaluate the tumor volume under two conditions: (i) without applying any detection threshold, where all tumor mass within the computational domain is included in the volume calculation; and (ii) with a T_2 -weighted MRI threshold, where only regions with tumor cell density exceeding 16% of the carrying capacity are considered part of the detectable volume. Figure 2 illustrates an example of these two cases, showing the tumor region identified with a T_2 threshold (solid red line) and without a threshold (dashed red line), for a simulation in which the tumor evolved without treatment for 12 weeks. Results of the tumor volume evolution over time, without (left panel) and with (right panel) application of the detection threshold, for the different treatment protocols are shown in Figure 3. From this figure, it is evident that for most treatment protocols ($D_T = 15, 20, 25, 30$), applying the T_2 detection threshold not only underestimates the actual tumor volume, but also suggests a transient complete remission ($V_T \approx 0$) lasting several weeks after therapy. In contrast, the results without threshold application reveal that a small residual tumor population survives in all cases, indicating that complete eradication is not achieved under any of the tested protocols. Specifically, in the T_2 -threshold simulations, treatments with $D_T = 15, 20, 25$, and 30 show a temporary remission

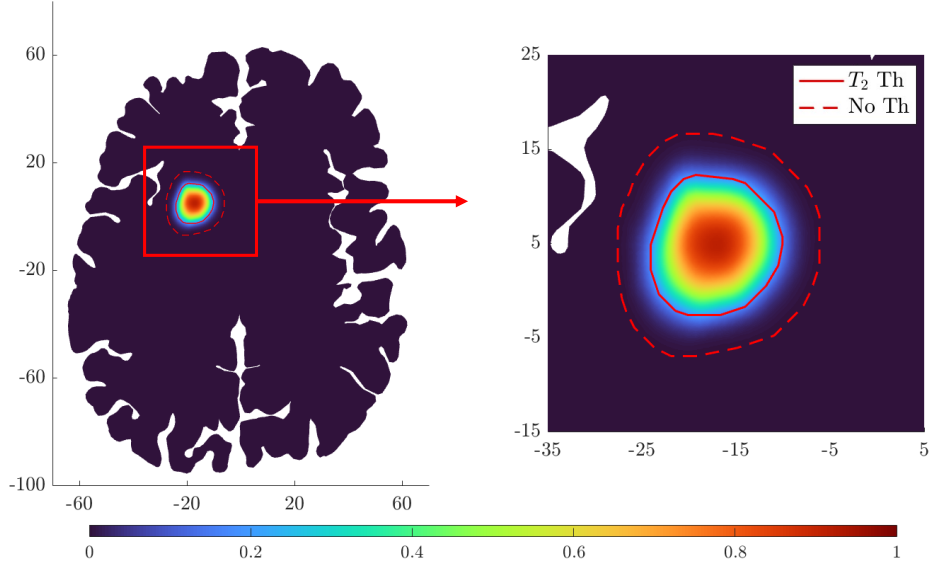


Figure 2: **Tumor area contour.** Identification of the tumor-occupied region in a brain slice with (solid red line) and without (dashed red line) application of the T_2 detection threshold. The tumor distribution results from a 12-week simulation of the model without treatment, starting from the initial conditions given in (24)–(25). The right plot shows a magnification of the main area affected by the tumor.

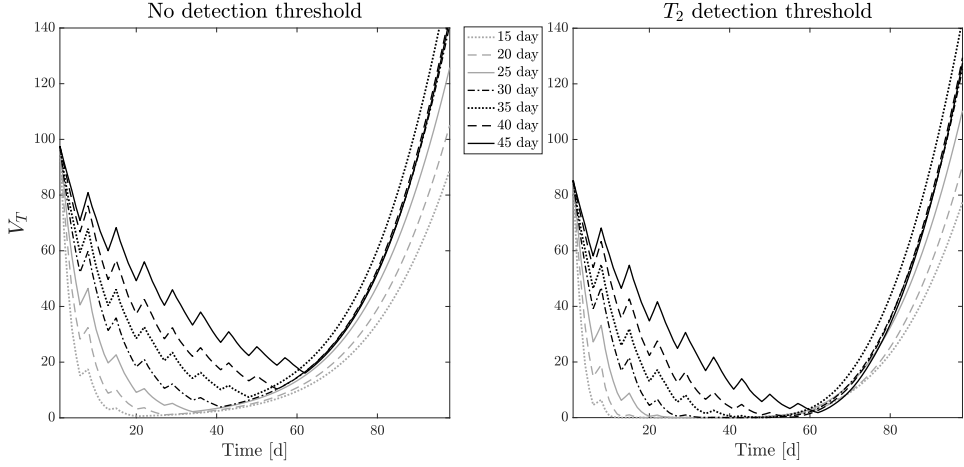


Figure 3: **Impact of the detection threshold on tumor volume quantification.** Comparison of simulated mean tumor volume (V_T) over time with (right panel) and without (left panel) application of the T_2 detection threshold for the different treatment protocols. In the figure legend the number D_T of days for each treatment is indicated. Mean tumor volumes were obtained by averaging the results of 200 independent simulations of the same experiment.

period of 1–4 weeks, followed by renewed tumor growth. When the full tumor mass is considered (no threshold), all treatment schedules exhibit eventual regrowth after therapy cessation. In the supplementary Figures A1, A2 we report the evolution of the mean tumor volume together with the minimum and maximum values obtained from 200 independent simulations of the same experiment for all analyzed treatment protocols. Analyzing the overall effect of the different treatment schedules, the longest delay in tumor recurrence is observed for $D_T = 15$ and $D_T = 20$, whereas protocols with $D_T = 30, 40$, and 45 produce comparable, yet less favorable outcomes.

4.2 Assessment of therapy efficacy: TCP/NTCP and R-score analysis

To enable a more robust and reliable interpretation of the tumor volume analysis presented in Section 4.1, the results must be considered alongside the potential toxicity associated with each fractionation scheme [73]. Accordingly, to evaluate the therapeutic trade-offs between tumor control and normal tissue damage, we employ three standard radiobiological metrics: tumor control probability (TCP), normal tissue complication probability (NTCP), and uncomplicated tumor control probability (UTCP) (see, e.g., [77]). Radiation therapy, in fact, represents a double-edged sword: while it effectively damages tumor cells, it inevitably affects normal tissue as well - albeit to a lesser extent. The ultimate goal is therefore to identify treatment protocols that maximize TCP while minimizing NTCP, thereby achieving high therapeutic efficacy with limited toxicity. These metrics are defined as follows.

- The tumor control probability quantifies the likelihood of complete tumor eradication and can be defined as

$$\text{TCP}(t) := \frac{\# \text{ simulations with } \tau_M \leq t}{\text{total } \# \text{ simulations}}$$

where τ_M denotes the first time point at which the cancer cell density M falls below 2% of the carrying capacity across the entire PTV region.

- The normal tissue complication probability estimates the probability of radiation-induced normal tissue injury and can be defined as

$$\text{NTCP}(t) := \frac{\# \text{ simulations with } \tau_Q \leq t}{\text{total } \# \text{ simulations}}$$

where τ_Q is defined as the first time point at which the healthy tissue density Q decreases below 30% of its original value within a subregion of the PTV of non-zero measure.

- The uncomplicated tumor control probability combines the previous two metrics to describe the probability of achieving effective tumor control without severe normal tissue complications, and is defined as

$$\text{UTCP}(t) := \text{TCP}(t)[1 - \text{NTCP}(t)]$$

assuming independence between TCP and NTCP.

The results of these metrics for the different treatment protocols are presented in Figure 4. From

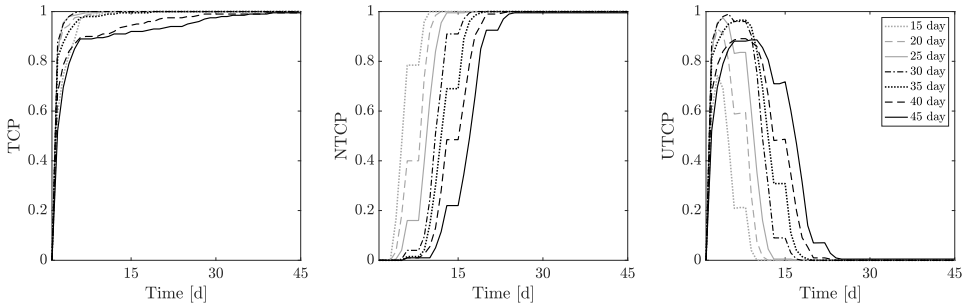


Figure 4: **TCP, NTCP, and UTCP.** Comparison of the mean TCP (left panel), NTCP (middle panel), and UTCP (right panel) evolution over time for the different treatment protocols. In the figure legend the number of D_T for each treatment is indicated. Mean values for TCP, NTCP, and UTCP were obtained by averaging the results of 200 independent simulations of the same experiment.

in this figure, we observe that the tumor response across the different treatment protocols, in terms of TCP, is quite similar and shows a high probability of tumor eradication within a relatively short time window (approximately 0–15 days), except for the hyper-fractionated schedules corresponding to $D_T = 40$ and $D_T = 45$. However, the corresponding NTCP results indicate that the hypo-fractionated treatments with $D_T = 15$ and $D_T = 20$ lead to faster and more severe normal tissue damage. These findings should be interpreted in light of the results presented in Figure 3, where $D_T = 15$ and

$D_T = 20$ achieved the greatest reduction in tumor volume, albeit at the cost of increased normal tissue toxicity, as reflected by the NTCP evolution. When considering both tumor control and toxicity together through the UTCP metric (Figure 4), intermediate fractionation schedules, such as $D_T = 25$, $D_T = 30$, or $D_T = 35$, emerge as the most balanced options, providing substantial tumor control while limiting adverse effects on normal tissue. For completeness, the temporal evolution of the mean TCP values, along with their corresponding standard deviations for all treatment protocols, are presented in Figure A3.

The UTCP metric has been adopted by several authors to rank treatment plans [78], [79]. However, as pointed out in [80], where it is referred to as the S -score, this metric exhibits some undesirable properties. In particular, for a fixed value of TCP, proportional changes in the absolute value of the NTCP for two competing treatment plans may alter their relative ranking. To address this limitation, Brenner [81] proposed the R -score index, defined as

$$R\text{-score} = \frac{TCP}{NTCP},$$

In the present work, we adopt this metric to rank the proposed treatment plans. Specifically, since TCP and NTCP are defined as functions of time in our framework, we introduce a cumulative R -score, defined as

$$R\text{-score} = \sum_{t=1}^{45} \frac{TCP(t)}{NTCP(t) + \epsilon}.$$

where t is expressed in days ([d]). We modify the denominator of Brenner's formula by introducing a small parameter ϵ to ensure mathematical correctness in cases where NTCP becomes zero. Since ϵ is assumed to be very small (specifically, we set $\epsilon = 10^{-3}$), it does not affect the therapy assessment. To enable a relative comparison among treatment schedules rather than an assessment of their absolute efficacy, the R -score is normalized by the maximum achieved value. The resulting normalized index lies in the interval $[0, 1]$, with higher values corresponding to more favorable treatment plans. Results of the R -score analysis are shown in Figure 5.

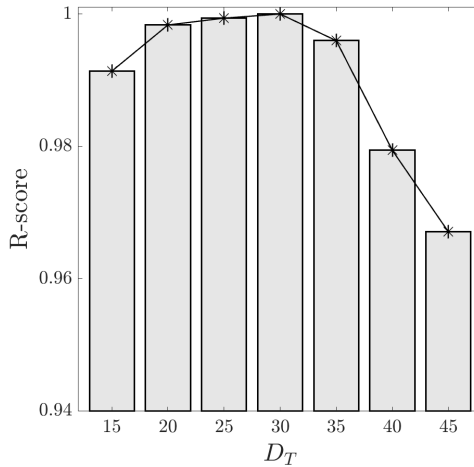


Figure 5: **R-score analysis.** R-score distribution for the different treatment protocols, with D_T values shown on the x-axis.

From Figure 5, we observe that the treatments achieving the best outcome in terms of the R -score correspond to D_T values between 20 and 35, with the optimal value obtained at $D_T = 30$, which coincides with the standard therapy. However, the differences with settings relying on $D_T = 20$ and $D_T = 25$ are relatively small. This finding partially aligns with the results of the TCP/NTCP analysis and the tumor volume assessment. In particular, it appears that more hyper-fractionated schedules yield lower R -scores, consistent with the observed length of tumor recurrence (see Figure 3), where the least favorable outcomes occur for $D_T = 40$ and $D_T = 45$.

4.3 RECIST-based analysis of tumor response

As a second numerical experiment, we assess the tumor response to the different treatment protocols using the Response Evaluation Criteria in Solid Tumors (RECIST) framework [82], [83]. According to this classification, we define: complete response (CR) as the disappearance of all target lesions; partial response (PR) as a reduction of at least 65% in the pre-treatment tumor volume; progressive disease (PD) as an increase of at least 73% in the pre-treatment tumor diameter; and stable disease (SD) as any change that does not meet the above criteria. Gliomas, due to their strong radioresistance and infiltrative growth, are typically classified clinically within the PD–PR range, with response primarily evaluated on T2-weighted images [14]. Here, we quantify the tumor response using the percentage tumor volume reduction at time $t = \tau$, defined as

$$RV_T(\tau) := \frac{(V_T(t=0) - V_T(t=\tau))}{V_T(t=0)} \times 100,$$

where V_T denotes the total tumor volume. We evaluate this metric at two distinct time points: $\tau = \tau_1$, corresponding to the last day of treatment, and $\tau = \tau_2$, corresponding to the follow-up period, defined as four weeks after the end of the treatment. For each case, $RV_T(\tau)$ is computed under two different assumptions: (i) without applying any detection threshold, and (ii) by applying a T_2 detection threshold for tumor volume estimation. The results are summarized in Figure 6. Specifically, Figure 6 compares the evolution of $RV_T(\tau)$ across the different treatment protocols, characterized by varying values of D_T , both without a detection threshold (left column) and with a T_2 detection threshold (right column). Results are shown at two time points: at the end of treatment ($\tau = \tau_1$, first row) and after the follow-up period ($\tau = \tau_2$, second row). Examining the results at the end of the treatment protocols, we observe that when the imaging detection threshold is applied, nearly all protocols (except for $D_T = 45$) appear, on average, to meet the CR criterion, indicating complete tumor eradication with a 100% reduction in tumor volume after therapy. However, this apparent success is largely an artifact caused by the limited sensitivity of imaging in capturing the full tumor extent, as evident in the left panel of the first row of Figure 6. In fact, when no detection threshold is applied, we note that from $D_T = 25$ onward, RV_T values begin to decline, revealing that the tumor mass is not fully eradicated. Nonetheless, across all cases, the average response remains within the PR category, indicating a partial, but consistent, response to treatment. After the four-week follow-up period (second row of Figure 6), the comparison between the left and right panels mirrors the previous findings: the use of a T_2 detection threshold results in a clear overestimation of treatment efficacy. Interestingly, despite this overestimation, all protocols show disease progression after follow-up, yet the mean response generally remains within the stable disease (SD) range. Only the minimum response values for $D_T = 35, 40$, and 45 fall into the PD region. Moreover, the standard therapeutic protocol ($D_T = 30$) consistently remains within the partial response (PR) range in both evaluation cases. These results are consistent with clinical observations of glioma evolution, which typically range between PD and PR classifications.

4.4 Evaluation of post-treatment relapse time

As a final numerical experiment, we evaluate the tumor response to the different treatment protocols using the post-treatment relapse time as a quantitative comparison metric. We define the relapse time (τ_R) as the minimum number of days between the start of therapy and the time at which the tumor regains its pre-treatment volume, measured without applying any detection threshold [14]. In addition, we introduce the adapted relapse time ($\bar{\tau}_R$), defined as the minimum number of days after the end of treatment required for the tumor to reach its pre-treatment volume. Relapse times for all treatment protocols are summarized in Figure 7. From the results presented in Figure 7, we first observe an apparent improvement in post-treatment relapse time for increasing hyper-fractionated treatment protocols (ranging from $D_T = 15$ to $D_T = 30$), while the response tends to stabilize for schedules with $D_T > 30$. This suggests that hyper-fractionated treatments are generally more effective in prolonging the relapse period, with consistent results even for the lowest-dose hyper-fractionation schemes. However, when comparing the relapse time (τ_R) with the adapted relapse time ($\bar{\tau}_R$), clear differences emerge. The metric $\bar{\tau}_R$ considers only the number of days after the end of therapy during which the tumor remains below its pre-treatment volume, whereas τ_R also includes the treatment days within this interval. When focusing exclusively on the post-treatment phase ($\bar{\tau}_R$),

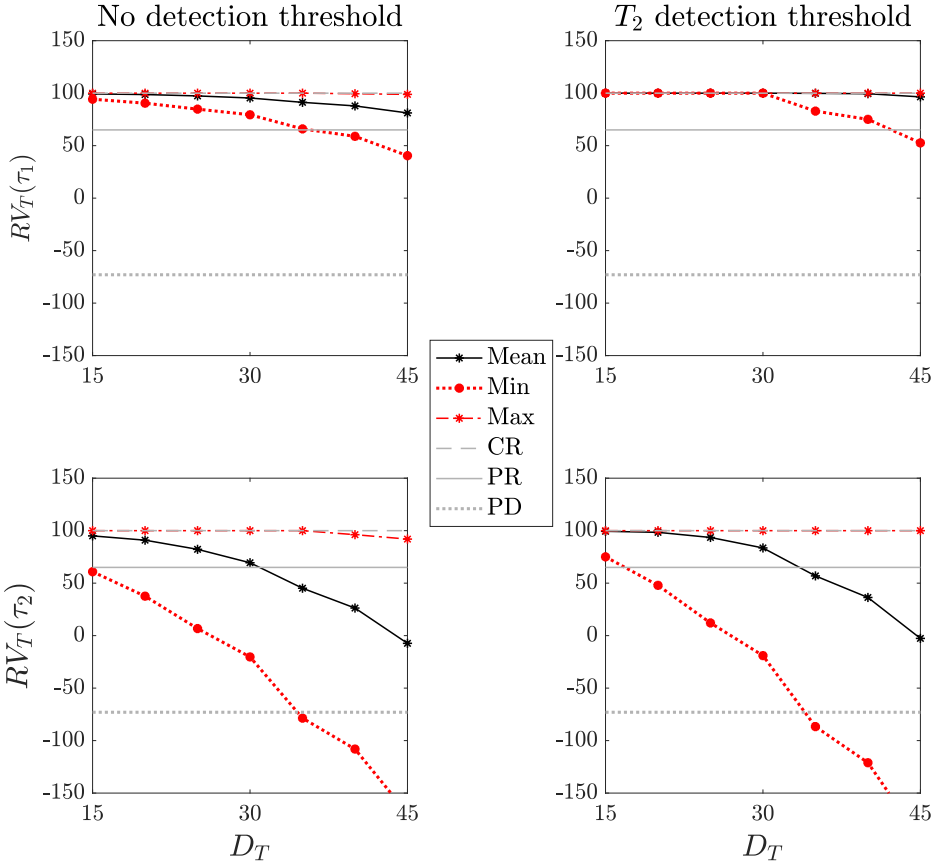


Figure 6: **Treatment efficacy based on RECIST criteria.** Evolution of the percentage tumor volume reduction ($RV_T(\tau)$) as a function of D_T , evaluated at the end of the treatment ($\tau = \tau_1$, first row) and after the follow-up period ($\tau = \tau_2$, second row). Results are shown both without a detection threshold (left column) and with a T_2 detection threshold (right column). The mean percentage tumor volume reduction is shown (black line/dots), together with the minimum (red dotted line) and maximum (red dashed line) values obtained from 200 independent simulations. The dashed grey line indicates the complete response (CR) threshold; the region between the dashed and solid grey lines corresponds to partial response (PR); the region between the solid and dotted grey lines represents stable disease (SD); and values below the dotted line indicate progressive disease (PD).

we observe a marked reduction in efficacy for protocols with $D_T > 35$. Furthermore, within the range $D_T = 15\text{--}35$, relapse times are comparable across protocols, with similar outcomes between the conventional schedule ($D_T = 30$) and high-dose hypo-fractionation treatments ($D_T < 30$). Overall, the conventional daily fractionation protocol achieves the longest relapse time and therefore delays tumor regrowth the most, avoiding the sharp drop in efficacy with only a modest increase in dose per fraction.

5 Discussion

The model proposed in this work is designed to investigate the influence of different radiotherapy treatment protocols on glioma progression within the brain, with particular emphasis on how therapy-related randomness and imaging limitations can affect overall treatment outcomes. To our knowledge, this is the first continuous multiscale model that introduces stochasticity at the mesoscopic level in the therapy-related terms and then derives the corresponding random partial differential equations at the macroscopic scale, accounting for nonlinear, myopic self-diffusion and multiple taxis mechanisms. As such, it represents an advancement of the models presented in [35], [42]. However, the explicit incorporation of stochastic components constitutes the main novelty, enabling a randomness-aware—and therefore more realistic—interpretation of model predictions. Notably, our numerical experiments

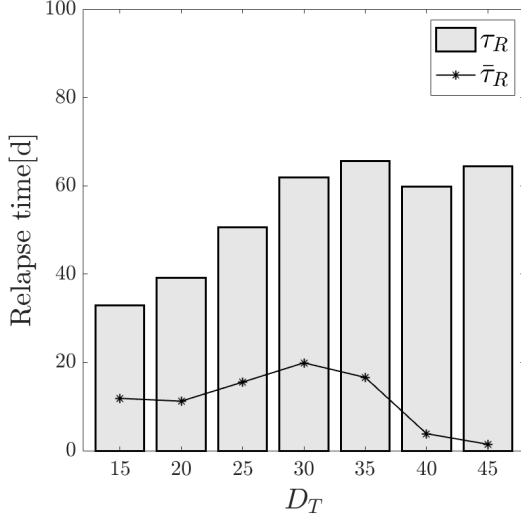


Figure 7: **Post-treatment relapse time.** Distribution of the mean relapse time (τ_R , vertical grey bars) and the adapted mean relapse time ($\bar{\tau}_R$, solid black line) for the different treatment protocols, with D_T values shown on the x-axis. Mean relapse times, obtained from 200 independent simulations, are expressed in days.

also employ evaluation metrics more closely aligned with clinical practice than those typically used in mathematical oncology.

We started from the description of single-cell dynamics of glioma cells interacting with (macroscopic) healthy and cancer cell densities, with the aim of implementing both an anti-crowding mechanism and a haptotactic movement response towards increasing tissue densities. We formulated the corresponding kinetic transport equations for the glioma distribution function on the mesoscopic scale. At this stage, we included both cell proliferation, triggered by cell receptor binding to tissue, and radiotherapy effects, which are modeled by means of a combination of the classical LQ radiobiological approach [27] and an Ornstein–Uhlenbeck process to represent mean-reverting random fluctuations in treatment efficacy. By upscaling the mesoscopic transport equations in a parabolic manner, we informally deduced the population-level system for the evolution of the glioma cell density and the normal tissue density. The normal tissue was thereby assumed to be degraded by tumor cells and radiation treatment. The resulting macroscopic system is a set of coupled random partial differential equations featuring diffusion-advection-reaction terms in the tumor equation and a simplified ODE-type dynamics (no motility terms) for the space-time evolution of tissue. Consistent with previous multiscale modeling works (e.g., [33], [34], [36], [39]), tumor migration is driven by terms carrying information from the microscopic scale. The myopic diffusion term involves a tumor diffusion tensor that explicitly accounts for the local tissue orientation. The haptotaxis term drives cells towards increasing tissue gradients, reflecting the cells’ tendency to follow dense tissue structures.

In the numerical experiments, we performed different tests aimed at addressing the tumor response to various treatment protocols using clinically-inspired settings and metrics. Specifically, we firstly utilized standard radiotherapy planning domains (i.e., GTV, CTV, and PTV) as reference regions. These domains reflect the radiological interpretation of imaging data and therewith associated detection thresholds, and they serve as the basis for evaluating tumor volume evolution over time. The detection threshold, which is related to imaging limitations, while not qualitatively changing the overall dynamics, leads to an underestimation of the tumor volume. More importantly, it introduces a temporal delay in identifying tumor relapse after the end of the treatment. Moreover, we assessed the tumor and normal tissue control probabilities (TCP and NTCP), enabling the exploration of therapeutic limitations related to the risk of severe normal tissue complications (NTCP). The use of these quantities as evaluation metrics demonstrated that intermediate fractionated treatment schedules (such as $D_T = 25$, $D_T = 30$, or $D_T = 35$) achieve a better balance between tumor control and adverse effects. This result is partially confirmed by the R -score analysis, which enables us to rank the treatment schedules and indicates better outcome for hypo-fractionated protocols compared to hyper-fractionated ones, with the best performance achieved by the standard schedule $D_T = 30$. Furthermore, tumor response to therapy was also evaluated using the Response Evaluation Crite-

ria in Solid Tumors (RECIST) [82]. The results obtained in this test were consistent with clinical observations of glioma evolution, which typically classify the response between progressive disease and partial response. Finally, by introducing a novel definition for the post-treatment relapse time ($\bar{\tau}_R$), we observed that the conventional daily fractionation protocol achieves the longest relapse time, thereby most effectively delaying tumor regrowth.

This work represents a first step toward a more detailed and realistic formulation of multiscale models that account for the effects of randomness in tumor outcomes. As such, it opens several directions for further development and future investigation. From a theoretical standpoint, some issues related to the existence and uniqueness of local solutions for the stochastic macroscopic system will be addressed in the forthcoming paper [50], although many questions remain open, for instance those concerning the existence of global solutions for our system. From a modeling perspective, a more detailed description of the evolution of tumor microenvironmental factors would be essential. For example, incorporating the dynamics of environmental acidity or hypoxia could provide insight into the potential development of therapy resistance. Moreover, combining radiotherapy with other therapeutic approaches (such as chemo- or immuno-therapy), in which randomness also plays a significant role, would be of great interest and would contribute toward making the framework more robust and ultimately more suitable for clinical applications.

Acknowledgment

The authors gratefully acknowledge Hospital Galdakao-Usansolo (Galdakao, Spain) for providing the DTI dataset, as well as the clinicians Dr. Y. Dzierma (Rostock University Medical Center) and Dr. S. Knobe (Saarland University Medical Center) for their fruitful discussions and valuable suggestions. The research of MC has been carried out under the auspices of the National Group of Mathematical-Physics (GNFM-INdAM). MC was supported by the European Union and the Italian Ministry of University and Research through the PNRR project Young Researchers 2024-SOE *“Integrated Mathematical Approach to Tumor Interface Dynamics”* (CUP: E13C24002380006) and by the National Group of Mathematical Physics (GNFM-INdAM) through the INdAM–GNFM Project *“Multi-species non-Maxwellian Fokker-Planck models inferred from local non-equilibrium distributions”* (CUP E5324001950001). SAH acknowledges support from the Department of Mathematics at RPTU Kaiserslautern. This work was conducted in association with the CZS project *AI-CARE*, which focuses on the development of PDE-based AI models and scRNA-seq data integration for discovering novel targets for GBM treatment.

Data availability statement

All relevant data are within the manuscript and its Supporting Information files.

Competing interests

The authors declare that the research was conducted in the absence of any commercial or financial relationships that could be construed as a potential conflict of interest.

A Appendix: Supplementary Figures

We complement the analysis presented in Section 4.1 by incorporating additional data on the outcomes of the different treatment schedules. Specifically, we exploit the stochastic characteristics of the proposed model to evaluate the impact of the detection threshold on tumor volume quantification in terms of mean (black solid line), minimum (blue dotted line), and maximum (blue dashed line) values obtained from 200 independent simulations of the same experiment. Figure A1 and A2 shows these results: the two rows display the tumor volume quantification without (top row) and with (bottom row) the application of the T_2 detection threshold, while the columns correspond to the different treatment protocols. The number of treatment days (D_T) for each protocol is indicated in the title of the respective panel. Figure A1 displays the results for $D_T = \{15, 20, 25, 30\}$, while Figure A2 displays the results for $D_T = \{35, 40, 45\}$. These figures allow us to observe the large variability in possible treatment outcomes, which is fully consistent with clinical reality. On average, none of the treatments succeeds in eradicating the tumor. In fact, although the radiotherapy protocols considered

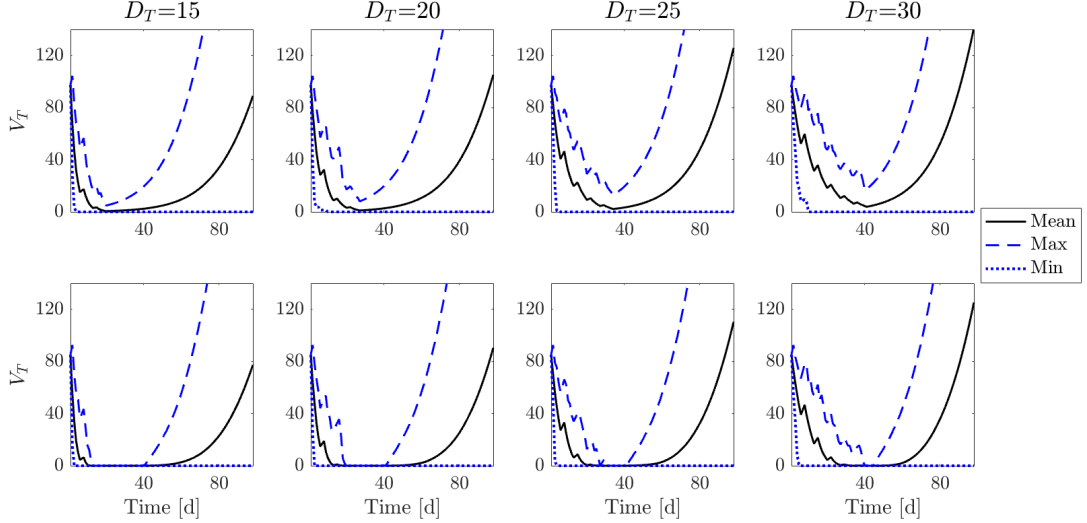


Figure A1: Impact of the detection threshold on tumor volume quantification - Part 1. Comparison of simulated tumor volume (V_T) evolution over time without (top row) and with (bottom row) application of the T_2 detection threshold across different treatment protocols. Each column corresponds to a treatment characterized by the number of treatment days D_T , as indicated in the respective panel title. For each case, the mean tumor volume (black line) is shown together with the minimum (dotted blue line) and maximum (dashed blue line) values obtained from 200 independent simulations of the same experiment.

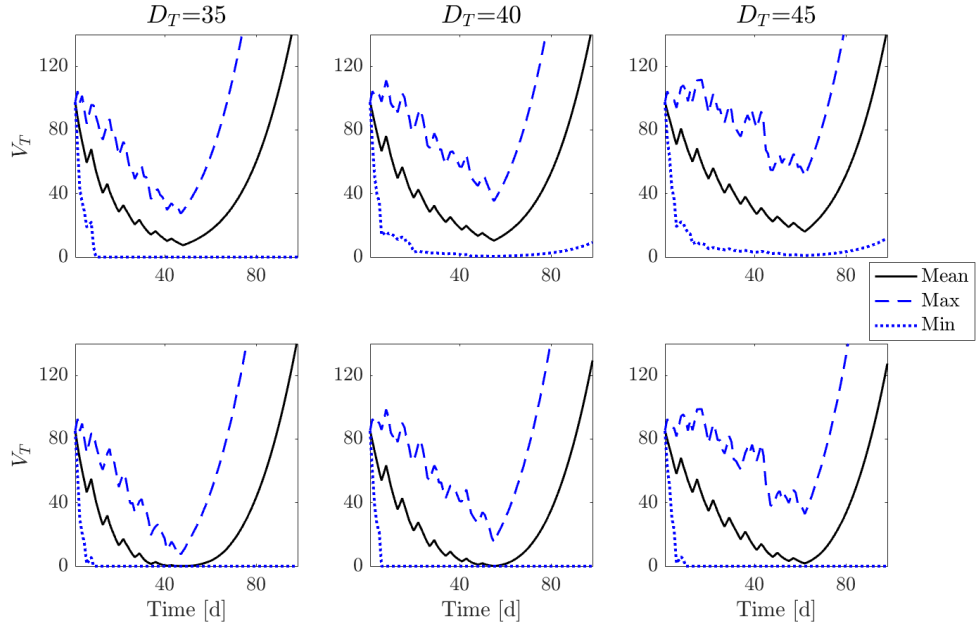


Figure A2: Impact of the detection threshold on tumor volume quantification - Part 2. Comparison of simulated tumor volume (V_T) evolution over time without (top row) and with (bottom row) application of the T_2 detection threshold across different treatment protocols. Each column corresponds to a treatment characterized by the number of treatment days D_T , as indicated in the respective panel title. For each case, the mean tumor volume (black line) is shown together with the minimum (dotted blue line) and maximum (dashed blue line) values obtained from 200 independent simulations of the same experiment.

here belong to the current standard of care for gliomas, it is well known that radiotherapy alone is rarely sufficient to eliminate the disease and that patients' prognosis often remains very poor.

Considering the analysis presented in Section 4.2 on the evolution of the tumor control probability (TCP) for the different treatment protocols, we include here an additional figure (Figure A3) that

highlights, alongside the mean TCP values for each D_T , the corresponding standard deviation computed from a set of 200 independent simulations of the same experiment. The results show that the variability is particularly high for smaller D_T indicating a strong stochastic influence on treatment outcomes in these cases.

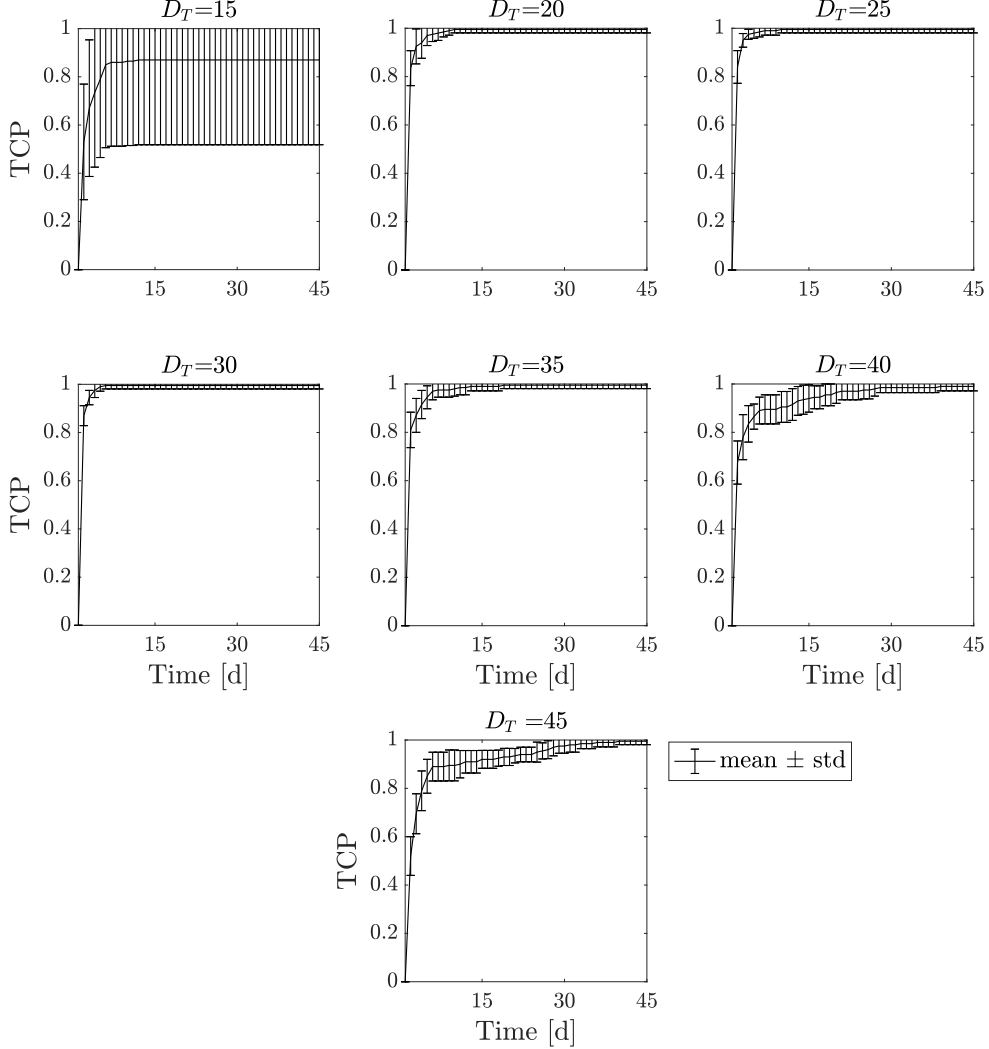


Figure A3: TCP evolution for different treatment protocols. Comparison of TCP evolution for the different treatment protocols. Each panel corresponds to a treatment characterized by the number of treatment days D_T , as indicated in the respective panel title. For each case, the mean \pm standard deviation TCP values are shown. Results are obtained from 200 independent simulations of the same experiment.

References

- [1] M. Wrensch, Y. Minn, T. Chew, M. Bondy, and M. S. Berger, “Epidemiology of primary brain tumors: Current concepts and review of the literature,” *Neuro-oncology*, vol. 4, no. 4, pp. 278–299, 2002.
- [2] Q. T. Ostrom, L. Bauchet, F. G. Davis, I. Deltour, J. L. Fisher, C. E. Langer, M. Pekmezci, J. A. Schwartzbaum, M. C. Turner, K. M. Walsh, et al., “The epidemiology of glioma in adults: A “state of the science” review,” *Neuro-oncology*, vol. 16, no. 7, pp. 896–913, 2014.
- [3] W. Wick, M. Osswald, A. Wick, and F. Winkler, “Treatment of glioblastoma in adults,” *Therapeutic advances in neurological disorders*, vol. 11, p. 1756 286 418 790 452, 2018.

- [4] M. E. Berens and A. Giese, “... those left behind.” biology and oncology of invasive glioma cells,” *Neoplasia*, vol. 1, no. 3, pp. 208–219, 1999.
- [5] V. Gondi, “Radiotherapy intensification for glioblastoma: Enhancing the backbone of treatment,” *Chinese clinical oncology*, vol. 10, no. 4, pp. 39–39, 2021.
- [6] C. Nieder, U. Nestle, R. Ketter, H. Kolles, S. J. Gentner, W. I. Steudel, and K. Schnabel, “Hyperfractionated and accelerated-hyperfractionated radiotherapy for glioblastoma multiforme,” *Radiation Oncology Investigations: Clinical and Basic Research*, vol. 7, no. 1, pp. 36–41, 1999.
- [7] T. H. Beckham, M. K. Rooney, M. F. McAleer, A. J. Ghia, M. C. Tom, S. Perni, S. McGovern, D. Grosshans, C. Chung, C. Wang, et al., “Hypofractionated radiotherapy for glioblastoma: A large institutional retrospective assessment of 2 approaches,” *Neuro-Oncology Practice*, vol. 11, no. 3, pp. 266–274, 2024.
- [8] J.-C. Trone, A. Vallard, S. Sotton, M. Ben Mrad, O. Jmour, N. Magné, B. Pommier, S. Laporte, and E. Ollier, “Survival after hypofractionation in glioblastoma: A systematic review and meta-analysis,” *Radiation oncology*, vol. 15, no. 1, p. 145, 2020.
- [9] M. R. Junntila and F. J. De Sauvage, “Influence of tumour micro-environment heterogeneity on therapeutic response,” *Nature*, vol. 501, no. 7467, pp. 346–354, 2013.
- [10] I. Telarovic, R. H. Wenger, and M. Pruschy, “Interfering with tumor hypoxia for radiotherapy optimization,” *Journal of Experimental & Clinical Cancer Research*, vol. 40, no. 1, p. 197, 2021.
- [11] B. Segedin and P. Petric, “Uncertainties in target volume delineation in radiotherapy—are they relevant and what can we do about them?” *Radiology and oncology*, vol. 50, no. 3, p. 254, 2016.
- [12] B. Winey and M. Bussiere, “Geometric and dosimetric uncertainties in intracranial stereotactic treatments for multiple nonisocentric lesions,” *Journal of applied clinical medical physics*, vol. 15, no. 3, pp. 122–132, 2014.
- [13] M. Conte, S. Casas-Tinto, and J. Soler, “Modeling invasion patterns in the glioblastoma battlefield,” *PLoS computational biology*, vol. 17, no. 1, e1008632, 2021.
- [14] R. Rockne, E. Alvord Jr, J. K. Rockhill, and K. R. Swanson, “A mathematical model for brain tumor response to radiation therapy,” *Journal of mathematical biology*, vol. 58, no. 4, pp. 561–578, 2009.
- [15] K. R. Swanson, E. C. Alvord Jr, and J. D. Murray, “A quantitative model for differential motility of gliomas in grey and white matter,” *Cell proliferation*, vol. 33, no. 5, pp. 317–329, 2000.
- [16] K. R. Swanson, R. C. Rockne, J. Claridge, M. A. Chaplain, E. C. Alvord Jr, and A. R. Anderson, “Quantifying the role of angiogenesis in malignant progression of gliomas: In silico modeling integrates imaging and histology,” *Cancer research*, vol. 71, no. 24, pp. 7366–7375, 2011.
- [17] H. L. Harpold, E. C. Alvord Jr, and K. R. Swanson, “The evolution of mathematical modeling of glioma proliferation and invasion,” *Journal of Neuropathology & Experimental Neurology*, vol. 66, no. 1, pp. 1–9, 2007.
- [18] S. A. Hiremath, C. Surulescu, A. Zhigun, and S. Sonner, “On a coupled sde-pde system modeling acid-mediated tumor invasion,” *Discrete and Continuous Dynamical Systems-Series B*, vol. 23, no. 6, pp. 2339–2369, 2018.
- [19] S. A. Hiremath and C. Surulescu, “Mathematical models for acid-mediated tumor invasion: From deterministic to stochastic approaches,” in *Multiscale Models in Mechano and Tumor Biology: Modeling, Homogenization, and Applications*, Springer, 2018, pp. 45–71.
- [20] S. A. Hiremath and C. Surulescu, “A stochastic model featuring acid-induced gaps during tumor progression,” *Nonlinearity*, vol. 29, no. 3, p. 851, 2016.
- [21] S. Hiremath and C. Surulescu, “A stochastic multiscale model for acid mediated cancer invasion,” *Nonlinear Analysis: Real World Applications*, vol. 22, pp. 176–205, 2015.
- [22] D. Katsaounis, M. A. J. Chaplain, and N. Sfakianakis, “Stochastic differential equation modelling of cancer cell migration and tissue invasion,” *Journal of Mathematical Biology*, vol. 87, no. 1, 2023.

- [23] E. A. B. F. Lima, R. C. Almeida, and J. T. Oden, “Analysis and numerical solution of stochastic phase-field models of tumor growth,” *Numerical Methods for Partial Differential Equations*, vol. 31, no. 2, 552–574, 2014.
- [24] S. Essarout, Z. Mahani, and S. Raghay, “Quantifying uncertainty of a mathematical model of drug transport in tumors,” *Mathematical Modeling and Computing*, vol. 9, no. 3, 567–578, 2022.
- [25] M. B. A. Mansour, H. S. Hussien, and A. H. Abobakr, “Numerical simulations of wave patterns in a stochastic partial differential equation model of tumor growth and invasion,” *Differential Equations and Dynamical Systems*, vol. 33, no. 3, 1069–1082, 2025.
- [26] S. Jerez and J. A. Cantó, “A stochastic model for the evolution of bone metastasis: Persistence and recovery,” *Journal of Computational and Applied Mathematics*, vol. 347, 12–23, 2019.
- [27] J. F. Fowler, “The linear-quadratic formula and progress in fractionated radiotherapy,” *The British journal of radiology*, vol. 62, no. 740, pp. 679–694, 1989.
- [28] M. Kim, A. Ghate, and M. H. Phillips, “A stochastic control formalism for dynamic biologically conformal radiation therapy,” *European Journal of Operational Research*, vol. 219, no. 3, pp. 541–556, 2012.
- [29] F. Saberian, A. Ghate, and M. Kim, “A theoretical stochastic control framework for adapting radiotherapy to hypoxia,” *Physics in Medicine & Biology*, vol. 61, no. 19, p. 7136, 2016.
- [30] K. W. Fornalski, L. Dobrzynski, and M. K. Janiak, “A stochastic markov model of cellular response to radiation,” *Dose Response*, vol. 9, no. 4, pp. 477–496, 2011.
- [31] N. Bellomo, L. Gibelli, A. Quaini, and A. Reali, “Towards a mathematical theory of behavioral human crowds,” *Mathematical Models and Methods in Applied Sciences*, vol. 32, no. 02, pp. 321–358, 2022.
- [32] N. Bellomo, *Modeling Complex Living Systems*. Birkhäuser Boston, 2008.
- [33] M. Conte, Y. Dzierma, S. Knobe, and C. Surulescu, “Mathematical modeling of glioma invasion and therapy approaches via kinetic theory of active particles,” *Mathematical Models and Methods in Applied Sciences*, vol. 33, no. 05, pp. 1009–1051, 2023.
- [34] M. Conte and C. Surulescu, “Mathematical modeling of glioma invasion: Acid- and vasculature mediated go-or-grow dichotomy and the influence of tissue anisotropy,” *Applied Mathematics and Computation*, vol. 407, p. 126305, 2021.
- [35] M. Conte, L. Gerardo-Giorda, and M. Groppi, “Glioma invasion and its interplay with nervous tissue and therapy: A multiscale model,” *Journal of theoretical biology*, vol. 486, p. 110088, 2020.
- [36] C. Engwer, T. Hillen, M. Knappitsch, and C. Surulescu, “Glioma follow white matter tracts: A multiscale dti-based model,” *Journal of mathematical biology*, vol. 71, no. 3, pp. 551–582, 2015.
- [37] C. Engwer, A. Hunt, and C. Surulescu, “Effective equations for anisotropic glioma spread with proliferation: A multiscale approach and comparisons with previous settings,” *Mathematical medicine and biology: a journal of the IMA*, vol. 33, no. 4, pp. 435–459, 2016.
- [38] E. Buckwar, M. Conte, and A. Meddah, “A stochastic hierarchical model for low grade glioma evolution,” *Journal of Mathematical Biology*, vol. 86, no. 6, p. 89, 2023.
- [39] C. Engwer, M. Knappitsch, and C. Surulescu, “A multiscale model for glioma spread including cell-tissue interactions and proliferation,” *Math Biosci Eng*, vol. 13, no. 2, pp. 443–460, 2016.
- [40] G. Corbin, A. Hunt, A. Klar, F. Schneider, and C. Surulescu, “Higher-order models for glioma invasion: From a two-scale description to effective equations for mass density and momentum,” *Mathematical Models and Methods in Applied Sciences*, vol. 28, no. 09, pp. 1771–1800, 2018.
- [41] G. Corbin, A. Klar, C. Surulescu, C. Engwer, M. Wenske, J. Nieto, and J. Soler, “Modeling glioma invasion with anisotropy-and hypoxia-triggered motility enhancement: From subcellular dynamics to macroscopic pdes with multiple taxis,” *Mathematical Models and Methods in Applied Sciences*, vol. 31, no. 01, pp. 177–222, 2021.
- [42] A. Hunt and C. Surulescu, “A multiscale modeling approach to glioma invasion with therapy,” *Vietnam Journal of Mathematics*, vol. 45, no. 1, pp. 221–240, 2017.

[43] P. Kumar and C. Surulescu, “A flux-limited model for glioma patterning with hypoxia-induced angiogenesis,” *Symmetry*, vol. 12, no. 11, p. 1870, 2020.

[44] P. Kumar, J. Li, and C. Surulescu, “Multiscale modeling of glioma pseudopalisades: Contributions from the tumor microenvironment,” *Journal of Mathematical Biology*, vol. 82, no. 6, p. 49, 2021.

[45] A. Dietrich, N. Kolbe, N. Sfakianakis, and C. Surulescu, “Multiscale modeling of glioma invasion: From receptor binding to flux-limited macroscopic PDEs,” *Multiscale Modeling and Simulation*, accepted, arXiv:2010.03277.

[46] K. Painter and T. Hillen, “Mathematical modelling of glioma growth: The use of diffusion tensor imaging (dti) data to predict the anisotropic pathways of cancer invasion,” *Journal of theoretical biology*, vol. 323, pp. 25–39, 2013.

[47] J. Kelkel and C. Surulescu, “A multiscale approach to cell migration in tissue networks,” *Mathematical Models and Methods in Applied Sciences*, vol. 22, no. 03, p. 1150017, 2012.

[48] T. Lorenz and C. Surulescu, “On a class of multiscale cancer cell migration models: Well-posedness in less regular function spaces,” *Mathematical Models and Methods in Applied Sciences*, vol. 24, no. 12, pp. 2383–2436, 2014.

[49] G. Chiari, M. Conte, and M. Delitala, “Multi-scale modeling of snail-mediated response to hypoxia in tumor progression,” *Communications in Nonlinear Science and Numerical Simulation*, vol. 145, p. 108673, 2025.

[50] S. Hiremath, M. Conte, and C. Surulescu, “Existence and uniqueness of solutions for stochastic treatment models of glioma invasion,” In preparation.

[51] Y. Tanaka, M. Oita, S. Inomata, T. Fuse, Y. Akino, and K. Shimomura, “Impact of patient positioning uncertainty in noncoplanar intracranial stereotactic radiotherapy,” *Journal of applied clinical medical physics*, vol. 21, no. 2, pp. 89–97, 2020.

[52] J. Becksfort, J. Uh, A. Saunders, J. A. Byrd, H. M. Worrall, M. Marker, C. Melendez-Suchi, Y. Li, J. Chang, K. Raghavan, et al., “Setup uncertainty of pediatric brain tumor patients receiving proton therapy: A prospective study,” *Cancers*, vol. 15, no. 22, p. 5486, 2023.

[53] J. W. Park, J. W. Yea, J. Park, and S. A. Oh, “Setup uncertainties and appropriate setup margins in the head-tilted supine position of whole-brain radiotherapy (wbrt),” *Plos one*, vol. 17, no. 8, e0271077, 2022.

[54] B. Oksendal, *Stochastic differential equations: an introduction with applications*. Springer Science & Business Media, 2013.

[55] L. Hlatky, P. Hahnfeldt, and R. Sachs, “Influence of time-dependent stochastic heterogeneity on the radiation response of a cell population,” *Mathematical Biosciences*, vol. 122, no. 2, pp. 201–220, 1994.

[56] H. Badri and K. Leder, “Optimal treatment and stochastic modeling of heterogeneous tumors,” *Biology direct*, vol. 11, no. 1, p. 40, 2016.

[57] T. Hillen, “M5 mesoscopic and macroscopic models for mesenchymal motion,” *Journal of mathematical biology*, vol. 53, no. 4, pp. 585–616, 2006.

[58] A. Zhigun and C. Surulescu, “A novel derivation of rigorous macroscopic limits from a micro-meso description of signal-triggered cell migration in fibrous environments,” *SIAM Journal on Applied Mathematics*, vol. 82, no. 1, pp. 142–167, 2022.

[59] R. G. Plaza, “Derivation of a bacterial nutrient-taxis system with doubly degenerate cross-diffusion as the parabolic limit of a velocity-jump process,” *Journal of mathematical biology*, vol. 78, no. 6, pp. 1681–1711, 2019.

[60] A. Shyntar and T. Hillen, “First and second moments of spherical distributions that are relevant for biological applications,” *Axioms*, vol. 14, no. 10, p. 743, 2025.

[61] M. Sidani, D. Wessels, G. Mouneimne, M. Ghosh, S. Goswami, C. Sarmiento, W. Wang, S. Kuhl, M. El-Sibai, J.-M. Backer, R. Eddy, D. Soll, and J. Condeelis, “Cofilin determines the migration behavior and turning frequency of metastatic cancer cells,” *Journal of Cell Biology*, vol. 179, no. 4, pp. 777–791, 2007.

[62] W. Diao, X. Tong, C. Yang, F. Zhang, C. Bao, H. Chen, L. Liu, M. Li, F. Ye, Q. Fan, and J. Wang, “Behaviors of glioblastoma cells in in vitro microenvironments,” *Scientific reports*, vol. 9, no. 1, pp. 1–9, 2019.

[63] D. Lauffenburger and J. Lindermann, *Receptors. Models for binding, trafficking and signaling.* Oxford University Press, 1993.

[64] L. Ke, Y. Shi, S. Im, X. Chen, and W. Yung, “The relevance of cell proliferation, vascular endothelial growth factor, and basic fibroblast growth factor production to angiogenesis and tumorigenicity in human glioma cell lines,” *Clinical Cancer Research*, vol. 6, no. 6, pp. 2562–2572, 2000.

[65] A. Bhatia, R. Moreno, A. S. Reiner, S. Nandakumar, H. S. Walch, T. M. Thomas, P. J. Nicklin, Y. Choi, A. Skakodub, R. Malani, et al., “Tumor volume growth rates and doubling times during active surveillance of idh-mutant low-grade glioma,” *Clinical Cancer Research*, vol. 30, no. 1, pp. 106–115, 2024.

[66] X. S. Qi, C. Schultz, and X. Li, “An estimation of radiobiologic parameters from clinical outcomes for radiation treatment planning of brain tumor,” *International Journal of Radiation Oncology, Biology, Physics*, vol. 64, no. 5, pp. 1570–1580, 2006.

[67] L. Barazzuol, N. Burnet, R. Jena, B. Jones, S. Jeffries, and N. Kirkby, “A mathematical model of brain tumour response to radiotherapy and chemotherapy considering radiobiological aspects,” *Journal of theoretical biology*, vol. 262, no. 3, pp. 553–565, 2010.

[68] J. Kroos, C. Stinner, C. Surulescu, and N. Surulescu, “SDE-driven modeling of phenotypically heterogeneous tumors: The influence of cancer cell stemness,” *Discrete and Continuous Dynamical Systems - Series B*, vol. 24, no. 8, p. 4629, 2019.

[69] V. Thomée, *Galerkin finite element methods for parabolic problems.* Springer Science & Business Media, 2007, vol. 25.

[70] U. M. Ascher, *Numerical methods for evolutionary differential equations.* SIAM, 2008.

[71] N. G. Burnet, S. J. Thomas, K. E. Burton, and S. J. Jeffries, “Defining the tumour and target volumes for radiotherapy,” *Cancer Imaging*, vol. 4, no. 2, p. 153, 2004.

[72] J. O’Donoghue, “The response of tumours with gompertzian growth characteristics to fractionated radiotherapy,” *International journal of radiation biology*, vol. 72, no. 3, pp. 325–339, 1997.

[73] W. Abou-Jaoudé and R. Dale, “A theoretical radiobiological assessment of the influence of radionuclide half-life on tumor response in targeted radiotherapy when a constant kidney toxicity is maintained,” *Cancer Biotherapy and Radiopharmaceuticals*, vol. 19, no. 3, pp. 308–321, 2004.

[74] M. Gerosa, A. Nicolato, and R. Foroni, “The role of gamma knife radiosurgery in the treatment of primary and metastatic brain tumors,” *Current opinion in oncology*, vol. 15, no. 3, pp. 188–196, 2003.

[75] T. E. Wheldon, C. Deehan, E. G. Wheldon, and A. Barrett, “The linear-quadratic transformation of dose–volume histograms in fractionated radiotherapy,” *Radiotherapy and Oncology*, vol. 46, no. 3, pp. 285–295, 1998.

[76] S. J. Nelson and S. Cha, “Imaging glioblastoma multiforme,” *The Cancer Journal*, vol. 9, no. 2, pp. 134–145, 2003.

[77] P. N. McDermott, *Tutorials in Radiotherapy Physics: Advanced Topics with Problems and Solutions.* CRC Press, 2016.

[78] S. A. Leibel, G. J. Kutcher, L. B. Harrison, D. E. Fass, C. M. Burman, M. A. Hunt, R. Mohan, L. J. Brewster, C. C. Ling, and Z. Y. Fuks, “Improved dose distributions for 3d conformal boost treatments in carcinoma of the nasopharynx,” *International Journal of Radiation Oncology* Biology* Physics*, vol. 20, no. 4, pp. 823–833, 1991.

[79] A. Chaikh, C. Khamphan, T. Kumar, R. Garcia, and J. Balosso, “What should we know about photon dose calculation algorithms used for radiotherapy? their impact on dose distribution and medical decisions based on tcp/ntcp,” *Int J Cancer Ther Oncol*, vol. 4, no. 4, p. 4418, 2016.

- [80] M. Langer, S. S. Morrill, and R. Lane, “A test of the claim that plan rankings are determined by relative complication and tumor-control probabilities,” *International Journal of Radiation Oncology* Biology* Physics*, vol. 41, no. 2, pp. 451–457, 1998.
- [81] D. J. Brenner and R. K. Sachs, “A more robust biologically based ranking criterion for treatment plans,” *International Journal of Radiation Oncology. Biology. Physics*, vol. 43, no. 3, pp. 697–697, 1999.
- [82] A. Padhani and L Ollivier, “The recist criteria: Implications for diagnostic radiologists,” *The British journal of radiology*, vol. 74, no. 887, pp. 983–986, 2001.
- [83] P. Therasse, S. G. Arbuck, E. A. Eisenhauer, J. Wanders, R. S. Kaplan, L. Rubinstein, J. Verweij, M. Van Glabbeke, A. T. van Oosterom, M. C. Christian, et al., “New guidelines to evaluate the response to treatment in solid tumors,” *Journal of the national cancer institute*, vol. 92, no. 3, pp. 205–216, 2000.